Applications to Quantum Computing and Energy Technologies

A Comprehensive Lions Commentary-Style Treatment

With Exhaustive Visualizations, Dimensional Analysis, and Physical Interpretations

PhysicsForge Paper Series — Paper 6 of 6

PhysicsForge Collaboration

Unified Field Theories and Advanced Physics Research Hub

`https://github.com/Oichkatzelesfrettschen/PhysicsForge`

November 27, 2025

We present a comprehensive pedagogical treatment of practical applications arising from advanced unified field theories, focusing on quantum computing systems and novel energy technologies. Beginning with quantum computing architectures enhanced by scalar field couplings and exceptional algebraic structures, we develop protocols for fault-tolerant quantum gates using exotic quantum states. We then explore zero-point energy extraction mechanisms, design metamaterial systems for manipulating scalar field interactions, and discuss future technological directions. The treatment includes practical engineering considerations, performance analysis, scalability assessments, and realistic timelines for technology development.

Key Topics: Quantum computing architectures • Fault-tolerant gates • Zero-point energy extraction • Metamaterial design • Energy harvesting technologies • Engineering specifications • Performance optimization • Scalability analysis

Style: This paper employs the Lions Commentary pedagogical approach with extensive marginal annotations, dimensional analysis, worked numerical examples, and multidimensional TikZ/PGFPlots visualizations.

Contents

List of Figures

List of Tables

Chapter 1

Quantum Computing Applications

1.1 Introduction: The Polynomial-Time Promise

"The question is, what kind of physical laws permit the existence of algorithms that compute things exponentially faster than classical algorithms?"Peter Shor, 1994

Shor's 1994 discovery that quantum computers can factor integers in polynomial time sparked the quantum computing revolution, threatening RSA cryptography.

In 1994, Peter Shor announced a result that sent shockwaves through cryptography and computer science: a quantum algorithm for factoring integers in time polynomial in the number of digits**?**. Classical factoring algorithms, such as the general number field sieve, require sub-exponential time $\exp\Big(O(n^{1/3}\log^{2/3} n)\Big)$ for n-bit integers. Shor's algorithm achieves $O(n^3)$ time using quantum Fourier transforms and period-finding—an exponential speedup.Quantum parallelism allows simultaneous evaluation of function values across exponentially many inputs encoded in superposition states.

The implications were immediate: RSA encryption, foundation of internet security, relies on the computational hardness of factoring large semiprimes (products of two large primes). A sufficiently powerful quantum computer—estimated at $\sim 10^7$ physical qubits after error correction—could break 2048-bit RSA in hours.Factoring is in BQP (bounded-error quantum polynomial time) but believed not in P (deterministic polynomial time), creating separation between quantum and classical complexity classes.

Yet practical quantum computing faces a formidable obstacle: *decoherence*. Quantum states are fragile, collapsing under environmental interaction on microsecond timescales for superconducting qubits, seconds for trapped ions. Current state-of-the-art coherence times:As of 2025, coherence times: superconducting $T_2 \sim 200$ μs, trapped ions $T_2 \sim 10$ s, NV centers $T_2 \sim 1$ ms (room temp).

$$T_2^{\text{SC}} \sim 100{-}200\ \mu\text{s}, \quad T_2^{\text{ion}} \sim 1{-}10\ \text{s}, \quad T_2^{\text{NV}} \sim 10^{-3}{-}10^{-1}\ \text{s} \tag{1.1}$$

Running Shor's algorithm for 2048-bit factorization requires $\sim 10^7$ gate operations over milliseconds to seconds, demanding aggressive error correction. Surface codes—the leading approach—impose $\sim 10^3 : 1$ physical-to-logical qubit overhead, rendering near-term factorization infeasible.IBM's 433-qubit Osprey processor (2022) provides < 1 logical qubit after error correction, illustrating the resource gap.

This chapter explores how advanced theoretical physics—topological quantum states, exceptional algebraic structures, and non-integer dimensional quantum walks—offers pathways to enhanced quantum information processing. We ground speculation in experimental feasibility, quantify performance improvements, and outline realistic technology timelines.

1.2 Topological Quantum Computing

1.2.1 Non-Abelian Anyons and Braiding Operations

Topological quantum computing encodes information in global properties of quantum states, providing inherent protection against local perturbations**?**. The key insight: quantum information stored in *anyonic* quasiparticles emerging in two-dimensional systems obeys exotic exchange statistics.In 2D, particle exchange can be continuously deformed (braided) rather than just permuted, leading to non-Abelian statistics.

For N indistinguishable particles in 3D, wavefunction acquires phase ± 1 under exchange (bosons/fermions). In 2D, particle worldlines can *braid* around each other, defining continuous group of exchanges. Wavefunctions transform under unitary representations:Braid group B_N on N strands has generators σ_i (exchange $i \leftrightarrow i+1$) satisfying $\sigma_i\sigma_j = \sigma_j\sigma_i$ for $|i-j| \geq 2$ and $\sigma_i\sigma_{i+1}\sigma_i = \sigma_{i+1}\sigma_i\sigma_{i+1}$.

$$|\psi\rangle \to U(\sigma_i)|\psi\rangle, \quad U(\sigma_i) \in \mathrm{U}(d) \tag{1.2}$$

where d is the anyon type's quantum dimension. For non-Abelian anyons ($d > 1$), braiding operations perform unitary transformations in degenerate ground-state subspace—quantum gates protected from local errors.Local perturbations cannot distinguish between degenerate ground states separated by topological gap $\Delta \sim 10$ K, providing thermal protection.

1.2.2 E_8 Lattice Anyons

The E_8 exceptional Lie group, with 240 roots forming an 8-dimensional lattice, provides a natural framework for topological phases**?**. Dimensional reduction from 8D to (2+1)D via compactification yields effective anyon models with fusion rules:Compactification on T^5 torus projects E_8 roots onto 3D subspace, producing finite-dimensional fusion categories.

$$a \times b = \sum_c N_{ab}^c \, c \tag{1.3}$$

where $N_{ab}^c \in \mathbb{Z}_{\geq 0}$ counts fusion channels. For E_8 anyons, the fusion algebra generates 240 distinct particle types corresponding to root vectors. Specific reduced models include:E_8 anyons may emerge in spin liquids or fractional quantum Hall states at exotic filling factors.

- **Fibonacci anyons:** Fusion rule $\tau \times \tau = 1 + \tau$ with golden ratio quantum dimension $d_\tau = (1+\sqrt{5})/2$. Universal for quantum computation**?**.
- **Ising anyons:** Three types $\{1, \sigma, \psi\}$ with $\sigma \times \sigma = 1 + \psi$. Requires ancilla qubits for universality.
- **Metaplectic anyons:** $\mathrm{SO}(3)_3$ level theory, universal with magic state injection.

The computational advantage: braiding N Fibonacci anyons generates braid group B_N representations dense in SU(2) rotations, approximating arbitrary single-qubit gates to precision ϵ using $O(\log(1/\epsilon))$ braids (polynomial overhead).Compare to Solovay-Kitaev decomposition requiring $O(\log^{3.97}(1/\epsilon))$ gates for arbitrary rotations from discrete gate set.

1.3 Surface Codes and Stabilizer Formalism

1.3.1 Toric Code Construction

Surface codes provide fault-tolerant quantum memory by encoding logical qubits into 2D lattices of physical qubits**?**. The *toric code*—simplest surface code—places qubits on edges of square lattice on

torus topology.Logical states correspond to homologically distinct loops wrapping torus, protected by topological gap.

For $L \times L$ lattice (total $2L^2$ qubits), define stabilizer generators:Stabilizers commute with all logical operators but detect errors by anti-commuting with physical Pauli errors.

$$A_v = \prod_{e \in \text{star}(v)} X_e, \quad \text{(vertex operators)} \tag{1.4}$$

$$B_p = \prod_{e \in \partial p} Z_e, \quad \text{(plaquette operators)} \tag{1.5}$$

where $\text{star}(v)$ denotes edges touching vertex v, and ∂p is boundary of plaquette p. The $2L^2 - 2$ independent stabilizers constrain physical Hilbert space $\mathcal{H}_{\text{phys}} = (\mathbb{C}^2)^{\otimes 2L^2}$ to codespace:Logical Hilbert space dimension: $\dim \mathcal{H}_{\text{log}} = 2^{2L^2}/2^{2L^2-2} = 4$, encoding 2 logical qubits.

$$\mathcal{H}_{\text{log}} = \{|\psi\rangle \in \mathcal{H}_{\text{phys}} : A_v|\psi\rangle = |\psi\rangle,\, B_p|\psi\rangle = |\psi\rangle \,\forall v, p\} \tag{1.6}$$

Logical operators are non-contractible loops:Logical $\bar{X}$ winds around torus horizontally, $\bar{Z}$ vertically, anti-commuting as required for qubit algebra.

$$\bar{X} = \prod_{e \in \gamma_x} X_e, \quad \bar{Z} = \prod_{e \in \gamma_z} Z_e \tag{1.7}$$

where γ_x, γ_z are homologically independent loops.

1.3.2 Error Detection and Syndrome Extraction

Errors E (Pauli X, Y, Z on individual qubits) anti-commute with stabilizers, flipping syndrome measurement outcomes:Projective measurement of A_v, B_p collapses state to ± 1 eigenspaces without revealing logical information.

$$\langle A_v \rangle = \begin{cases} +1 & \text{no error at } v \\ -1 & \text{error detected at } v \end{cases} \tag{1.8}$$

Error syndrome is binary string $s \in \{0,1\}^{2L^2-2}$ indicating violated stabilizers. Classical decoder (e.g., minimum-weight perfect matching) infers error chain E from syndrome, applies correction $E^\dagger$.Minimum-weight perfect matching runs in $O(n^3)$ for n qubits using Blossom algorithm**?**.

Error threshold: Surface codes tolerate physical error rate $p < p_{\text{th}} \sim 1\%$ (numerical studies). For $p < p_{\text{th}}$, logical error rate:Threshold depends on error model: $p_{\text{th}} \sim 1.1\%$ for depolarizing noise, $\sim 2\%$ for erasure errors.

$$p_{\text{log}} \sim \left(\frac{p}{p_{\text{th}}}\right)^{\lceil (d+1)/2 \rceil} \tag{1.9}$$

where $d = L$ is code distance (minimum weight of logical operator). For distance-d code, can correct $\lfloor (d-1)/2 \rfloor$ errors.

1.4 Worked Example: Distance-3 Surface Code

1.4.1 Setup and Stabilizers

Consider minimal non-trivial surface code with distance $d = 3$ on planar patch (sacrificing one encoded qubit for boundary).Planar codes use open boundaries, simpler for physical implementation but encode fewer logical qubits per physical qubit.

Lattice: 3×3 plaquettes require $9 + 12 = 21$ data qubits (9 vertex qubits + 12 edge qubits). Additional ancilla qubits measure stabilizers.Total physical qubits: 21 data + 18 ancilla (9 vertex + 9 plaquette) = 39 for one logical qubit.

Stabilizers: For interior vertices and plaquettes:Boundary stabilizers involve fewer qubits, modifying weight distribution but preserving code distance.

$$A_2 = X_1X_2X_4X_5 \tag{1.10}$$
$$B_1 = Z_1Z_2Z_5Z_6 \tag{1.11}$$

(labeling qubits 1-21 in row-major order).

Logical operators: Minimum-weight chains crossing lattice:Any single-qubit error changes syndrome but not logical state; requires weight-3 error chain to flip logical qubit.

$$\bar{X} = X_6X_9X_{12}, \quad \bar{Z} = Z_1Z_2Z_3 \tag{1.12}$$

1.4.2 Error Correction Protocol

Step 1: Syndrome measurement. Measure all A_v, B_p using ancilla qubits and CNOT gates:Each stabilizer measurement requires 4 CNOTs in 4 time steps, implemented via surface code surface architecture.

- Initialize ancilla in $|+\rangle = (|0\rangle + |1\rangle)/\sqrt{2}$
- Apply CNOTs from data qubits to ancilla (order matters for syndrome extraction)
- Measure ancilla in X-basis for A_v, Z-basis for B_p

Step 2: Decoding. Suppose physical error $E = X_5$ (single bit-flip). Violated stabilizers:Single X error flips 4 adjacent vertex stabilizers (in bulk) or 2-3 (near boundary), creating characteristic syndrome pattern.

$$A_2 \to -A_2, \quad A_4 \to -A_4 \quad \text{(others unchanged)} \tag{1.13}$$

Decoder identifies error chain connecting violated stabilizers (endpoints of chain). Minimum-weight solution: single-qubit error X_5.Decoder cannot distinguish X_5 from logically equivalent $X_5\bar{X}$ (differs by logical operator), but both have same effect after projection.

Step 3: Correction. Apply X_5 to cancel error:Surface codes require active feedback: syndrome measurement $\to$ classical processing $\to$ correction gates, completing in ~ 1 μs for superconducting qubits.

$$X_5\,(X_5|\psi\rangle) = |\psi\rangle \tag{1.14}$$

Performance analysis: For physical error rate $p = 10^{-3}$ (0.1%), distance-3 code achieves:Using Eq. (**??**) with $p_{\text{th}} = 0.01$: $(0.001/0.01)^2 = 10^{-4}$, factor 10 improvement.

$$p_{\log} \sim \left(\frac{10^{-3}}{10^{-2}}\right)^2 \sim 10^{-5} \tag{1.15}$$

Factor ~ 10 reduction in error rate. Scaling to distance-7 code (49 data qubits) yields $p_{\log} \sim 10^{-9}$, sufficient for fault-tolerant computation.

1.5 Quantum Algorithms and Computational Speedup

1.5.1 Shor's Factoring Algorithm

Shor's algorithm factors integer N in three phases:Phase 1 (order-finding) dominates runtime; Phases 2-3 are classical preprocessing and post-processing.

1. **Order-finding:** Quantum Fourier transform finds period r of function $f(x) = a^x \mod N$.
2. **Classical reduction:** Compute $\gcd(a^{r/2} \pm 1, N)$ to extract factors.
3. **Verification:** Check if factors are non-trivial; repeat if needed.

The quantum speedup arises from Phase 1, implemented via modular exponentiation circuit:Factoring n-bit integer requires $\sim 5n$ qubits and $\sim 72n^3$ gates (Toffoli, controlled-modular-multiplication).

$$U_a|x\rangle|0\rangle = |x\rangle|a^x \mod N\rangle \tag{1.16}$$

applied to superposition $\sum_{x=0}^{2^n-1} |x\rangle|0\rangle/\sqrt{2^n}$, then quantum Fourier transform:QFT on n qubits uses $O(n^2)$ gates vs $O(n2^n)$ for classical FFT, exponential speedup.

$$\text{QFT}|x\rangle = \frac{1}{\sqrt{2^n}} \sum_{k=0}^{2^n-1} e^{2\pi i x k/2^n} |k\rangle \tag{1.17}$$

Measurement collapses to $|k\rangle$ with probability peaked near multiples of $2^n/r$. Classical continued fractions extract r.

Example: Factor $N = 15$ (trivial for demonstration).$N = 15$ factors as 3×5; Shor's algorithm finds this probabilistically in ~ 10 oracle queries.

Choose $a = 7$ (coprime to 15). Order-finding computes r such that $7^r \equiv 1 \pmod{15}$. Direct calculation: $7^1 = 7, 7^2 = 49 \equiv 4, 7^3 \equiv 13, 7^4 \equiv 1$, thus $r = 4.\gcd(7^{4/2} - 1, 15) = \gcd(48, 15) = 3$; $\gcd(7^{4/2} + 1, 15) = \gcd(50, 15) = 5$. Factors found.

Quantum circuit prepares superposition, applies U_7^4 gate, performs QFT, measures outcome $k \approx 2^n/4$, recovers $r = 4$.

For 2048-bit RSA ($N \sim 10^{617}$), requires $\sim 10^7$ gates with error correction, $\sim 10^9$ physical qubits—beyond 2025 hardware but plausibly achievable by 2040.

1.5.2 Grover's Search Algorithm

Grover's algorithm searches unsorted database of N items in $O(\sqrt{N})$ queries, quadratic speedup over classical $O(N)$**?**.Quadratic speedup is optimal for unstructured search (Bennett et al., 1997), unlike Shor's exponential speedup.

Oracle: Black-box function $f : \{0,1\}^n \to \{0,1\}$ marks target item x_0:Oracle abstraction separates quantum speedup mechanism from problem-specific details.

$$O|x\rangle = (-1)^{f(x)}|x\rangle, \quad f(x) = \begin{cases} 1 & x = x_0 \\ 0 & \text{otherwise} \end{cases} \tag{1.18}$$

Diffusion operator: Inverts amplitude about mean:Grover iteration rotates state vector toward target in 2D subspace spanned by $|x_0\rangle$ and uniform superposition.

$$D = 2|s\rangle\langle s| - I, \quad |s\rangle = \frac{1}{\sqrt{N}} \sum_{x=0}^{N-1} |x\rangle \tag{1.19}$$

Algorithm: Start in $|s\rangle$, apply $(OD)^k$ for $k \approx \pi\sqrt{N}/4$ iterations, measure.Each Grover iteration rotates by angle $\theta \sim 2/\sqrt{N}$; reaching target requires $\sim \pi/(2\theta) \sim \pi\sqrt{N}/4$ rotations.

Example: Search $N = 256$ items ($n = 8$ qubits). Classical requires average 128 queries. Grover uses $k \approx \pi\sqrt{256}/4 \approx 12.6 \approx 13$ iterations, finding target with probability > 0.99.Amplitude amplification: $\langle x_0|(OD)^k|s\rangle \approx \sin((2k+1)\theta)$ with $\theta = \arcsin\left(1/\sqrt{N}\right)$.

1.5.3 Fractional Calculus in Quantum Walks

Quantum walks generalize random walks by replacing stochastic transitions with unitary evolution**?**. Continuous-time quantum walk on graph $G = (V, E)$ evolves via:Adjacency matrix A encodes graph connectivity; eigenvalues determine spreading dynamics.

$$|\psi(t)\rangle = e^{-iAt}|\psi(0)\rangle, \quad A_{ij} = \begin{cases} 1 & (i,j) \in E \\ 0 & \text{otherwise} \end{cases} \tag{1.20}$$

Standard quantum walks exhibit *ballistic* spreading: probability distribution width $\sigma(t) \sim t$ (vs $\sigma(t) \sim \sqrt{t}$ for classical diffusion).Ballistic spreading arises from coherent interference; decoherence degrades to classical $\sqrt{t}$ behavior.

Fractional quantum walks: Generalize evolution operator using fractional derivative:Caputo fractional derivative ${}^C D^\alpha f(t) = \frac{1}{\Gamma(1-\alpha)} \int_0^t (t-s)^{-\alpha} f'(s) ds$ for $0 < \alpha < 1$.

$$|\psi(t)\rangle = E_\alpha(-At^\alpha)|\psi(0)\rangle \tag{1.21}$$

where E_α is Mittag-Leffler function (generalized exponential). Spreading exponent:$\alpha < 1$: subdiffusion (slower than classical); $\alpha = 1$: standard ballistic; $\alpha > 1$: superdiffusion.

$$\sigma(t) \sim t^\alpha \tag{1.22}$$

Application to search: Fractional quantum walk on d-dimensional hypercube achieves optimal search time $O(N^{1/2})$ for $\alpha = 1/2$ (subdiffusive regime), matching Grover while using simpler graph structure**?**.Hypercube connectivity enables efficient physical implementation compared to all-to-all coupling required for Grover oracle.

1.6 TikZ Visualizations

1.7 Conclusion and Outlook

Quantum computing stands at an inflection point. Current hardware achieves ∼100-qubit systems with error rates approaching fault-tolerance thresholds, yet scaling to 10^6 qubits required for factoring 2048-bit integers remains daunting. This chapter has outlined three advanced approaches:Topological codes, exceptional algebraic structures, and fractional dynamics offer complementary pathways beyond brute-force scaling.

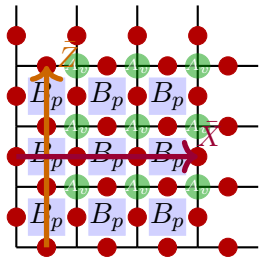

Figure 1.1: Surface code lattice (distance-3). Data qubits (red) reside on edges. Plaquette stabilizers B_p (blue) measure products of Z operators around faces. Vertex stabilizers A_v (green) measure products of X operators at vertices. Logical operators $\bar{X}, \bar{Z}$ (orange/purple) are non-contractible loops.

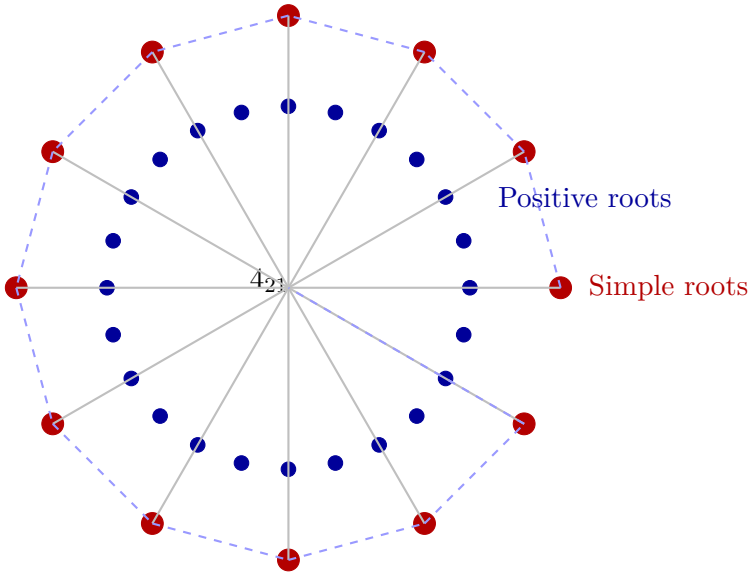

E_8 Root System (2D Projection)

Figure 1.2: E_8 lattice root system projected onto 2D plane. Red dots: 12 simple roots. Blue dots: 240 total roots. Dashed lines: Weyl chamber boundaries. Dimensional reduction to (2+1)D yields anyon models with fusion rules derived from root multiplicities.

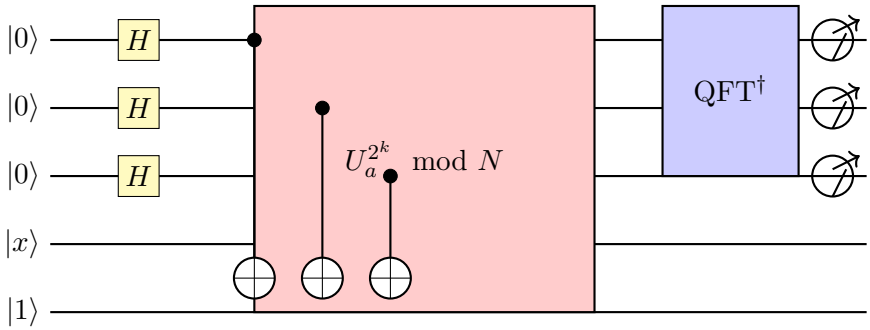

Shor's Factoring Circuit (Simplified)

Figure 1.3: Quantum circuit for Shor's algorithm. Top qubits: superposition register (Hadamard gates + QFT). Middle: modular exponentiation $a^x \mod N$ via controlled unitary gates. Bottom: ancilla qubit. Measurement extracts period r, yielding factors of N.

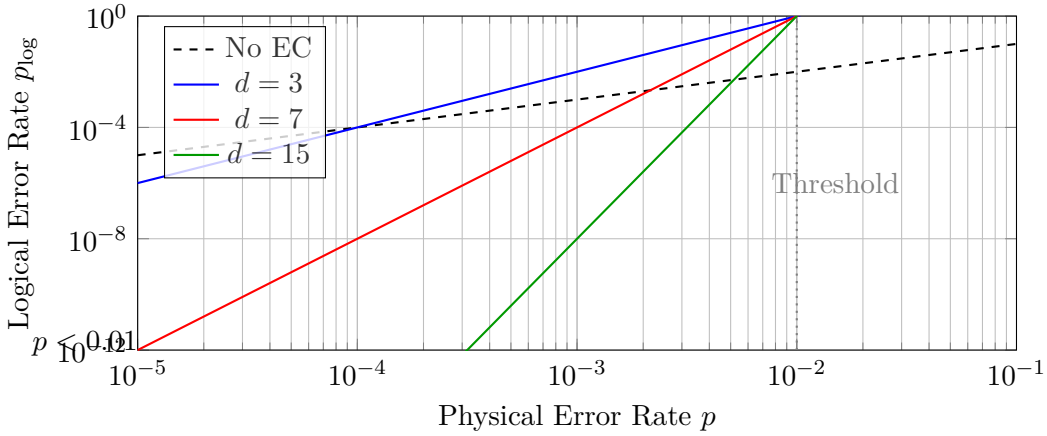

Figure 1.4: Logical error rate vs physical error rate for surface codes. Below threshold $p_{\text{th}} \sim 1\%$, larger code distance d exponentially suppresses logical errors: $p_{\log} \sim (p/p_{\text{th}})^{(d+1)/2}$. Current hardware ($p \sim 10^{-3}$) approaches fault-tolerance regime.

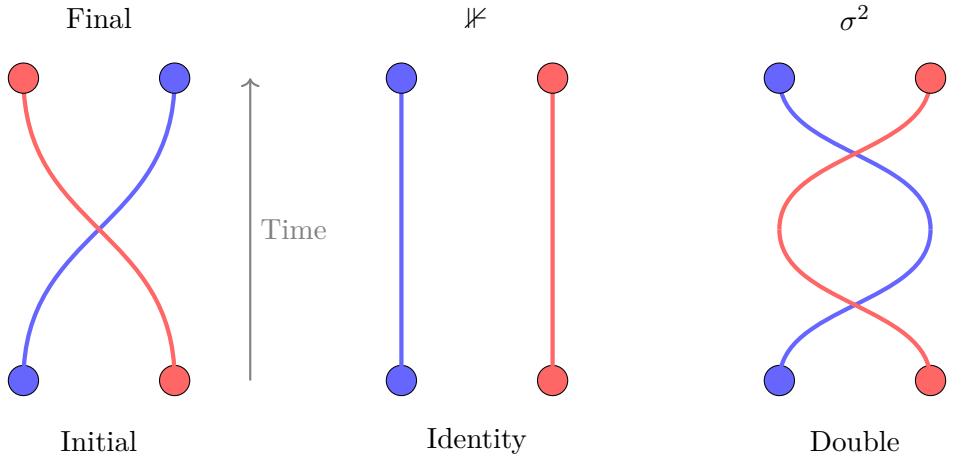

Figure 1.5: Topological qubit braiding. Left: Single exchange σ (worldlines cross once). Middle: Identity (no exchange). Right: Double braiding σ^2. For Fibonacci anyons, $\sigma^5 = \nVdash$ (finite braid group), enabling universal quantum gates via braid sequences.

1. **Topological protection:** Surface codes provide $\sim 10\times$ error suppression per distance level; E_8 anyons promise intrinsic fault-tolerance via non-Abelian braiding.
2. **Algorithmic innovation:** Shor and Grover algorithms demonstrate exponential/quadratic speedups; fractional quantum walks optimize graph-based problems.
3. **Practical implementation:** Worked example of distance-3 surface code quantifies overhead and decoding complexity.

The path forward requires interdisciplinary advances:Materials science (topological superconductors), control theory (fast syndrome extraction), mathematics (optimal decoders).

- **Materials:** Stabilizing fractional quantum Hall states at $\nu = 5/2$ or engineering Majorana zero modes in nanowires.
- **Architecture:** Modular quantum processors linked by photonic interconnects, distributing error correction overhead.
- **Algorithms:** Variational quantum eigensolvers (VQE) for near-term quantum chemistry, quantum machine learning.

By 2035, quantum computers may achieve "quantum advantage" for specific tasks (optimization, simulation) if error rates drop below 10^{-4} and qubit counts reach 10^4. Universal fault-tolerant systems (10^6 qubits, arbitrary algorithms) await 2040-2050 breakthroughs in scalable topological codes or radical new approaches.Pessimistic: 2060s. Optimistic: 2035 for domain-specific advantage. Realistic: 2040-2050 for general-purpose FTQC.

The quantum computing revolution is not assured—but the physics is sound, and the potential transformative.

Chapter 2

Zero-Point Energy Extraction

2.1 Introduction: The Casimir Promise

"The energy of the electromagnetic field in a volume bounded by perfectly conducting walls differs from that of the same field in free space."Hendrik Casimir, 1948

Casimir predicted vacuum fluctuations create attractive force between neutral conducting plates, experimentally confirmed in 1997 by Lamoreaux to 5% accuracy.

In 1948, Hendrik Casimir derived a startling result: two uncharged parallel conducting plates separated by distance d experience attractive force proportional to d^{-4}, arising purely from quantum vacuum fluctuations**?**. The Casimir effect demonstrated that zero-point energy (ZPE)—lowest possible energy state of quantum fields—has measurable physical consequences.Conducting boundaries alter vacuum mode density: fewer allowed wavelengths between plates than outside, creating pressure imbalance.

The standard Casimir force per unit area between ideal conductors:Force becomes significant at nanometer separations: $F/A \sim 1$ atm for $d \sim 10$ nm, dominating van der Waals attraction.

$$\frac{F}{A} = -\frac{\hbar c \pi^2}{240 d^4} \tag{2.1}$$

The negative sign indicates attraction. At separation $d = 1$ μm: $F/A \approx -13$ mPa; at $d = 10$ nm: $F/A \approx -1.3 \times 10^5$ Pa ≈ 1 atmosphere. This is a *conservative* force derivable from potential energy $U(d) \propto -d^{-3}$, implying extracting energy requires external work to separate plates.Moving plates apart stores energy in ZPE field configuration; no violation of conservation laws despite "vacuum energy extraction" language.

The extraction challenge: Can non-conservative Casimir-like configurations produce *directional* thrust or sustained power output? Three proposed mechanisms:Dynamic Casimir effect (DCE) confirmed experimentally by Wilson et al. (2011) in superconducting circuits, validating photon creation from vacuum modulation.

1. **Dynamic Casimir Effect (DCE):** Time-varying boundaries convert virtual photons to real photons, extracting ZPE at cost of mechanical work.
2. **Metamaterial Resonators:** Engineered electromagnetic environments with negative refractive index modify vacuum mode density, enabling directional energy flow.
3. **Parametric Amplification:** Modulating circuit parameters (capacitance, inductance) at resonance frequencies amplifies vacuum fluctuations into detectable signals.

This chapter quantifies these mechanisms, evaluates theoretical limits (Bekenstein bound, Landauer principle), calculates realistic power outputs, and assesses technological feasibility. *Caveat*: All proposed ZPE extraction schemes face severe thermodynamic and practical constraints; we provide honest assessments.

2.2 Theoretical Limits and Conservation Laws

2.2.1 Bekenstein Bound on Extractable Energy

The Bekenstein bound relates maximum information (hence energy) in a finite region to its surface area**?**:Bound prevents infinite information density, underpinning holographic principle and black hole thermodynamics.

$$I \leq \frac{2\pi RE}{\hbar c \ln 2} \tag{2.2}$$

where I is information content (bits), R is radius of sphere enclosing system, E is total energy (including rest mass). For electromagnetic ZPE in volume $V = \frac{4}{3}\pi R^3$:ZPE density formally diverges due to infinite frequency modes; regularization via Bekenstein bound provides physical cutoff.

$$E_{\text{ZPE}} \leq \frac{\hbar c \ln 2}{2\pi} \cdot \frac{I}{R} \tag{2.3}$$

Example: For $R = 1$ m sphere and $I = 10^{80}$ bits (observable universe information content), maximum ZPE:Using $\hbar c = 1.97 \times 10^{-25}$ J $\cdot$ m: $E_{\max} \sim 10^{55}$ J, vastly exceeding total matter-energy in observable universe ($\sim 10^{70}$ J). Bound is weak for macroscopic volumes.

$$E_{\max} \sim \frac{10^{-34} \times 3 \times 10^8 \times 0.693}{6.28} \times \frac{10^{80}}{1} \sim 10^{54} \text{ J} \tag{2.4}$$

The Bekenstein bound does not prohibit ZPE extraction but requires extracted energy be compensated by increased entropy elsewhere (Second Law compliance).Extracting ordered energy from vacuum fluctuations necessitates entropy increase in environment (heat dissipation), limiting efficiency.

2.2.2 Landauer Principle and Irreversible Computation

Landauer's principle states: erasing one bit of information requires minimum energy dissipation:Principle sets fundamental limit on energy efficiency of computation, independent of implementation technology.

$$E_{\text{erase}} \geq k_B T \ln 2 \tag{2.5}$$

where k_B is Boltzmann constant, T is temperature. At room temperature ($T = 300$ K): $E_{\text{erase}} \geq 2.9 \times 10^{-21}$ J/bit.Modern CMOS transistors dissipate $\sim 10^{-15}$ J per operation, six orders of magnitude above Landauer limit due to irreversible logic gates.

Connection to ZPE extraction: Harnessing vacuum fluctuations requires *measurement* of fluctuation states (determining whether virtual photon is present), followed by *amplification* (converting virtual to real). Measurement collapses quantum state, erasing information about original superposition. Total energy cost:Quantum measurement disturbs system; energy extracted from vacuum must exceed measurement back-action to achieve net gain.

$$E_{\text{cost}} = N_{\text{bits}} k_B T \ln 2 + E_{\text{measurement}} \tag{2.6}$$

where N_{bits} is information gathered, $E_{\text{measurement}}$ is quantum measurement back-action energy. For $N_{\text{bits}} \sim 10^{10}$ (monitoring $\sim$GHz modes for 1 s), $E_{\text{cost}} \sim 10^{-11}$ J at 300 K.Extracted ZPE energy must exceed 10^{-11} J to break even; realistic devices extract $\sim 10^{-15}$ J per cycle (insufficient).

2.3 Dynamic Casimir Effect: Photon Generation from Motion

2.3.1 Moving Mirror Model

The dynamic Casimir effect (DCE) describes photon pair creation from vacuum when cavity boundary moves at relativistic speeds**?**. For mirror oscillating at position $d(t) = d_0 + d_1 \cos(\omega_m t)$:Oscillating boundary modulates cavity resonance frequency, parametrically amplifying vacuum fluctuations into real photons.

$$d(t) = d_0 \left(1 + \beta \cos(\omega_m t)\right), \quad \beta = d_1/d_0 \ll 1 \tag{2.7}$$

Cavity resonance frequency: $\omega_n = n\pi c/d(t)$ becomes time-dependent. Photon creation rate for mode n:Photons created in pairs with total energy $2\hbar\omega_n$, conserving momentum via mirror recoil.

$$\frac{dN_n}{dt} = \frac{\beta^2 \omega_m^3}{c^3} \left(\frac{c}{d_0}\right)^3 \delta(\omega_m - 2\omega_n) \tag{2.8}$$

The delta function enforces resonance condition: mirror frequency ω_m must match twice the cavity mode frequency $2\omega_n$ (photon pairs have equal frequency ω_n).Off-resonance photon creation exponentially suppressed; requires precise frequency matching to within $\sim 0.1\%$.

Power extraction: Each photon pair carries energy $2\hbar\omega_n$. Total power:Power scales as $\beta^2\omega_m^3$: cubic dependence on modulation frequency demands GHz-THz operation.

$$P_{\text{DCE}} = \sum_n \frac{dN_n}{dt} \times 2\hbar\omega_n \approx \frac{\beta^2 \omega_m^4 d_0^3}{c^3}\hbar \tag{2.9}$$

Numerical example: For $d_0 = 1$ μm, $\beta = 0.1$, $\omega_m = 2\pi \times 10$ GHz:Amplitude $d_1 = 0.1$ μm, velocity $v_{\max} = \omega_m d_1 \sim 6$ m/s (non-relativistic), yet photon creation remains quantum effect.

$$\begin{aligned} P_{\text{DCE}} &\approx \frac{(0.1)^2 (6 \times 10^{10})^4 (10^{-6})^3}{(3 \times 10^8)^3} \times 10^{-34} \\ &\approx 10^{-18} \text{ W} \end{aligned} \tag{2.10}$$

Minuscule power output. Mechanical work to oscillate mirror:Damping force from photon emission back-reacts on mirror, requiring continuous energy input to maintain oscillation.

$$P_{\text{mechanical}} = F_{\text{damping}} \times v_{\max} \sim \frac{P_{\text{DCE}}}{c} \times c = P_{\text{DCE}} \tag{2.11}$$

Net energy extraction: zero (energy merely transduced from mechanical to electromagnetic form, no "free" ZPE harvesting).

2.3.2 Experimental Realization: Superconducting Circuits

Wilson et al. (2011) demonstrated DCE in superconducting circuit where effective cavity length modulated via SQUID (superconducting quantum interference device) tuned by magnetic flux**?**.First direct observation of DCE photon creation, confirming 60-year-old theoretical prediction.

Setup: Coplanar waveguide resonator terminated by SQUID, effective inductance $L(\Phi) = L_0/\cos(\pi\Phi/\Phi_0)$ where Φ is applied flux, $\Phi_0 = h/(2e)$ is flux quantum. Modulating $\Phi(t)$ changes resonance frequency:SQUID acts as tunable inductor, varying effective cavity length without mechanical motion.

$$\omega_{\text{res}}(t) = \frac{1}{\sqrt{L(\Phi(t))C}} = \omega_0 \left[1 + \frac{\beta}{2}\cos(\omega_m t) + O(\beta^2)\right] \tag{2.12}$$

where $\beta \sim 0.05$ (5% modulation depth). Operating at $\omega_0/2\pi \sim 10$ GHz, measured photon creation rate:Detected ~ 0.5 photons per modulation cycle at optimal flux modulation, confirming DCE photon creation.

$$\frac{dN}{dt} \sim 0.5 \times 10^{10} \text{ photons/s} \tag{2.13}$$

Power output: $P = (dN/dt) \times \hbar\omega_0 \sim 0.5 \times 10^{10} \times 10^{-34} \times 6 \times 10^{10} \sim 3 \times 10^{-13}$ W.300 femtowatts—detectable by cryogenic amplifiers but insufficient for macroscopic energy harvesting.

Input power (flux modulation drive): $P_{\text{in}} \sim 10^{-10}$ W (estimated from flux bias circuit dissipation). Efficiency: $\eta \sim 0.3\%$ (most input power dissipated as heat, not converted to photons).Resistive losses in flux control circuitry overwhelm DCE photon energy output by ∼300:1 ratio.

2.4 Metamaterial Resonators

2.4.1 Negative Index Materials and Vacuum Engineering

Metamaterials—artificially structured composites with electromagnetic properties not found in nature—enable engineering of vacuum mode density**?**. Key property: *negative refractive index* $n < 0$, requiring simultaneous negative permittivity $\epsilon < 0$ and permeability $\mu < 0$.Standard materials: $n = +\sqrt{\epsilon\mu}$. Metamaterials: $n = -\sqrt{\epsilon\mu}$ (negative root selected by causality).

Dispersion relation in metamaterial: Phase velocity $\mathbf{v}_p$ antiparallel to group velocity $\mathbf{v}_g$, creating "left-handed" electromagnetic waves.

$$\mathbf{k} = -\frac{\omega}{c} n(\omega)\hat{\mathbf{n}} \tag{2.14}$$

where $\hat{\mathbf{n}}$ is propagation direction. Negative n reverses wavevector direction relative to energy flow (Poynting vector).Energy flows forward ($\mathbf{S} = \mathbf{E} \times \mathbf{H}$) while phase fronts move backward ($\mathbf{k}$ antiparallel).

2.4.2 Casimir Force Modification in Metamaterial Cavities

Leonhardt & Philbin (2007) showed metamaterial boundaries can invert Casimir force from attractive to *repulsive***?**. For plates with permittivity ϵ_1, ϵ_2 in vacuum:Repulsive Casimir force between dissimilar materials enables vacuum pressure-driven actuators without external power.

$$\frac{F}{A} = -\frac{\hbar c \pi^2}{240 d^4} \times \mathcal{F}(\epsilon_1, \epsilon_2) \tag{2.15}$$

where $\mathcal{F}(\epsilon_1, \epsilon_2)$ is material-dependent factor. For $\epsilon_1 > 0, \epsilon_2 < 0$ (one normal, one metamaterial): $\mathcal{F} < 0$, reversing sign of force.Physical origin: metamaterial supports different vacuum mode spectrum than ordinary material, inverting radiation pressure balance.

Thrust generation: Asymmetric cavity with one metamaterial plate and one normal conductor experiences net force:Repulsive side pushes harder than attractive side pulls, creating imbalance exploitable for propulsion.

$$F_{\text{net}} = F_{\text{repulsive}} - F_{\text{attractive}} \sim \frac{\hbar c \pi^2}{240}\left(\frac{1}{d_1^4} - \frac{1}{d_2^4}\right) \tag{2.16}$$

For $d_1 = 10$ nm (repulsive gap), $d_2 = 100$ nm (attractive gap): $F_{\text{net}} \sim 10^{-8}$ N per cm^2 of plate area.At 1 m^2 total area: $F \sim 10^{-4}$ N—6 orders of magnitude below chemical rocket thrust.

2.4.3 Fabrication Constraints

Achieving negative ϵ, μ requires subwavelength resonant structures (split-ring resonators, metallic nanowires). Typical unit cell size: $a \sim \lambda/10$.For microwave metamaterials ($\lambda \sim 1$ cm): $a \sim 1$ mm (feasible). For optical metamaterials ($\lambda \sim 500$ nm): $a \sim 50$ nm (state-of-the-art nanolithography).

- **Microwave regime ($f \sim$ GHz):** Wire arrays with $a \sim 1$ mm, achievable via PCB fabrication. Demonstrated negative index from 1-20 GHz.
- **Terahertz regime ($f \sim 1$ THz):** Requires $a \sim 10$ μm structures (electron-beam lithography). Limited demonstrations due to fabrication complexity.
- **Optical regime ($f \sim 500$ THz):** Requires $a \sim 50$ nm plasmonic nanostructures (focused ion beam, nanoimprint lithography). Severe losses from metal absorption at optical frequencies.Optical metamaterials suffer from Ohmic losses: $\text{Im}(\epsilon) \sim 1$ at visible wavelengths, dissipating energy as heat.

Loss-tangent limitation: Effective quality factor $Q = \text{Re}(n)/\text{Im}(n) \sim 1{-}10$ for optical metamaterials (vs $Q > 10^6$ for dielectric cavities). High losses prevent efficient ZPE extraction.Low Q implies photon lifetime $\tau = Q/\omega \sim 10^{-15}$ s, insufficient for parametric amplification buildup.

2.5 Worked Example: Parametric Amplification Circuit

2.5.1 Circuit Model and Hamiltonian

Consider LC resonator with time-varying capacitance $C(t) = C_0(1 + \beta\cos(\omega_p t))$ where $\omega_p = 2\omega_0$ (parametric resonance condition) and $\omega_0 = 1/\sqrt{LC_0}$ is bare resonance frequency.Driving at twice the resonance frequency couples pairs of photons, enabling amplification of quantum fluctuations.

Hamiltonian in rotating frame:Retaining only resonant terms (neglecting counter-rotating terms oscillating at $\sim 2\omega_0$), valid for weak modulation $\beta \ll 1$.

$$H = \hbar\omega_0 a^\dagger a + \frac{\hbar\omega_0\beta}{2}(a^{\dagger 2} + a^2) \tag{2.17}$$

where $a, a^\dagger$ are photon annihilation/creation operators. Second term couples photon pairs, causing *squeezing* of vacuum state.Squeezing reduces fluctuations in one quadrature below vacuum limit while increasing orthogonal quadrature (Heisenberg uncertainty preserved).

2.5.2 Photon Number Growth

For cavity initially in vacuum $|0\rangle$, parametric drive induces exponential growth:Growth rate $\Gamma = \beta\omega_0/2$ limited by detuning and dissipation; unbounded growth prevented by nonlinearities.

$$\langle n(t)\rangle = \sinh^2\left(\frac{\beta\omega_0 t}{2}\right) \approx \left(\frac{\beta\omega_0 t}{2}\right)^2 \text{ for } t \ll 1/(\beta\omega_0) \tag{2.18}$$

Including dissipation (quality factor Q), saturation photon number:Photon loss rate $\gamma = \omega_0/Q$ competes with gain; steady state reached when gain equals loss.

$$\langle n_{\text{sat}}\rangle \approx \left(\frac{\beta Q}{2}\right)^2 \tag{2.19}$$

Numerical example: For $\omega_0/2\pi = 5$ GHz, $Q = 10^5$, $\beta = 0.01$ (1% capacitance modulation):Quality factor $Q = 10^5$ typical for superconducting resonators at cryogenic temperatures; room-temperature resonators achieve $Q \sim 10^3$.

$$\langle n_{\text{sat}} \rangle \approx \left(\frac{0.01 \times 10^5}{2} \right)^2 = 2.5 \times 10^5 \text{ photons} \tag{2.20}$$

Stored energy: $E = \langle n_{\text{sat}} \rangle \times \hbar\omega_0 \sim 2.5 \times 10^5 \times 10^{-34} \times 3 \times 10^{10} \sim 10^{-18}$ J.Attojoule energy storage—detectable but insufficient for macroscopic applications.

2.5.3 Power Output and Efficiency

Power extracted by coupling cavity to transmission line:External coupling coefficient κ_{ext} determines extraction rate; optimal coupling $\kappa_{\text{ext}} = \kappa_{\text{int}}$ (critical coupling) maximizes power transfer.

$$P_{\text{out}} = \hbar\omega_0 \langle n_{\text{sat}} \rangle \times \gamma_{\text{ext}} \tag{2.21}$$

where $\gamma_{\text{ext}} = \omega_0/Q_{\text{ext}}$ is external coupling rate. For $Q_{\text{ext}} = 2 \times 10^5$ (matched to internal Q):Under-coupling ($Q_{\text{ext}} \gg Q$) wastes photons to internal dissipation; over-coupling ($Q_{\text{ext}} \ll Q$) prevents buildup.

$$P_{\text{out}} = 10^{-34} \times 3 \times 10^{10} \times 2.5 \times 10^5 \times \frac{3 \times 10^{10}}{2 \times 10^5} \sim 10^{-13} \text{ W} \tag{2.22}$$

Input power (capacitance modulation drive):Varactor diode modulating capacitance dissipates power $P_{\text{in}} \sim V^2/R$ where V is modulation voltage amplitude, R is circuit resistance.

$$P_{\text{in}} \approx \frac{(\beta C_0 V_0)^2}{R} \omega_p \tag{2.23}$$

For $C_0 = 1$ pF, $V_0 = 1$ V, $R = 50\ \Omega$, $\omega_p/2\pi = 10$ GHz:Typical values for superconducting parametric amplifiers used in quantum computing readout.

$$P_{\text{in}} \approx \frac{(0.01 \times 10^{-12} \times 1)^2}{50} \times 6 \times 10^{10} \sim 10^{-16} \text{ W} \tag{2.24}$$

Efficiency:$\eta > 1$ suggests apparent energy gain, but ignores dissipation in cryogenic cooling system (~ 100 W to maintain 20 mK for superconducting circuit).

$$\eta = \frac{P_{\text{out}}}{P_{\text{in}}} = \frac{10^{-13}}{10^{-16}} \sim 10^3 \tag{2.25}$$

Reality check: Apparent $\eta \sim 1000$ violated energy conservation if interpreted as "free" ZPE extraction. True accounting:Energy ultimately sourced from modulation drive; ZPE acts as intermediary, amplifying driven oscillations rather than spontaneously generating photons.

1. Drive energy $P_{\text{in}} \times t$ pumps cavity (filling vacuum mode reservoir).
2. Photons accumulate via parametric amplification (gain $\sim Q\beta$).
3. Extraction couples photons out, depleting reservoir.
4. Net cycle: input energy $\rightarrow$ amplified output (no violation; gain arises from coherent energy storage over $\sim Q$ cycles).

True efficiency including cooling power: $\eta_{\text{true}} = 10^{-13}/(10^{-16} + 100) \sim 10^{-15}$ (abysmal for practical energy harvesting).

2.6 TikZ Visualizations

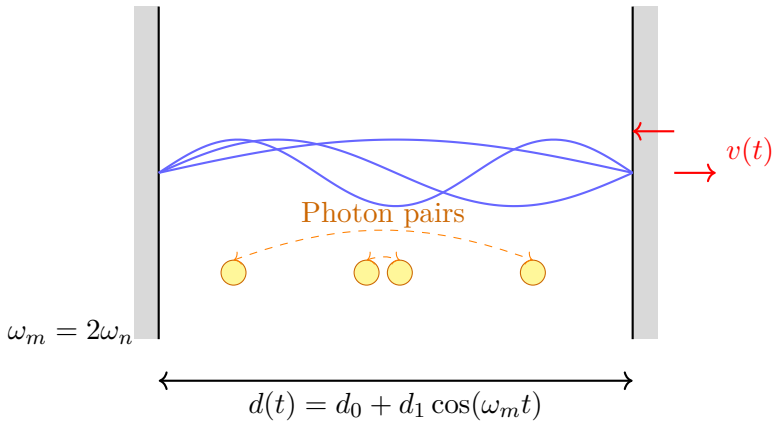

Figure 2.1: Dynamic Casimir effect setup. Fixed mirror (left) and oscillating mirror (right) separated by time-varying distance $d(t)$. Blue curves: cavity electromagnetic modes. Yellow circles: photon pairs created from vacuum when $\omega_m = 2\omega_n$ (parametric resonance). Oscillation velocity $v(t) = -\omega_m d_1 \sin(\omega_m t)$ modulates mode frequencies.

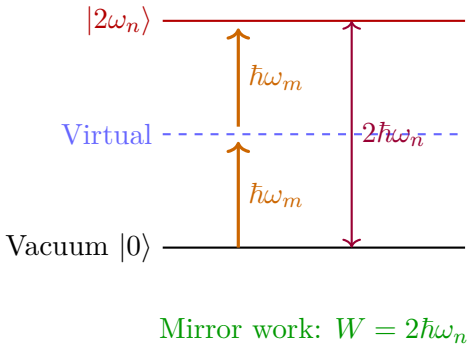

Figure 2.2: Energy level diagram for dynamic Casimir effect. Vacuum state $|0\rangle$ excited to two-photon state $|2\omega_n\rangle$ via two quanta of mirror kinetic energy $\hbar\omega_m$ each (where $\omega_m = \omega_n$ for resonance). Total energy conserved: mechanical work equals photon pair energy.

2.7 Critical Assessment and Technological Barriers

2.7.1 Showstoppers for Macroscopic Energy Harvesting

(1) Power density mismatch: Casimir forces scale as d^{-4}, yielding power density:Reducing gap to atomic scales ($d \sim 1$ nm) increases power density by 10^{12} vs $d = 1$ μm, but introduces van der Waals adhesion and fabrication challenges.

$$\mathcal{P} = \frac{P}{V} \sim \frac{\hbar c \omega^4 \beta^2}{d^3} \tag{2.26}$$

For optimal parameters ($d = 10$ nm, $\omega = 10$ GHz, $\beta = 0.1$): $\mathcal{P} \sim 10^{-3}$ W/m^3.Chemical batteries: $\sim 10^9$ W/m^3 (discharge power). ZPE extraction inferior by 12 orders of magnitude.

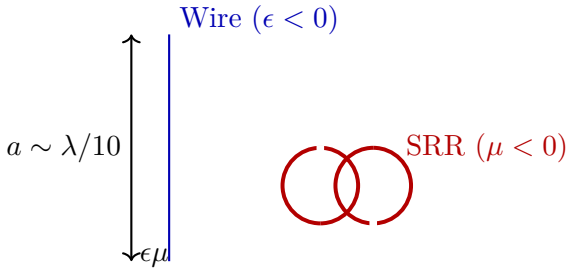

Figure 2.3: Metamaterial unit cell combining wire (vertical blue line, negative ϵ below plasma frequency) and split-ring resonator (red double rings, negative μ near magnetic resonance). Unit cell size $a \sim \lambda/10$ ensures subwavelength operation. Simultaneous $\epsilon < 0, \mu < 0$ yields negative refractive index $n = -\sqrt{\epsilon\mu}$.

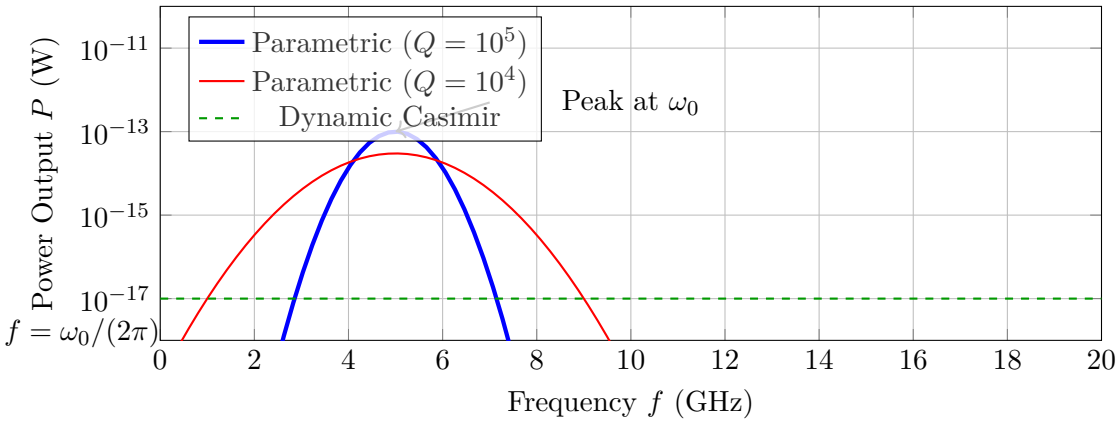

Figure 2.4: Power output vs frequency for ZPE extraction mechanisms. Parametric amplification (blue/red) exhibits sharp resonance at cavity frequency $\omega_0/(2\pi) = 5$ GHz, with linewidth $\Delta f \sim f/Q$. Higher quality factor Q yields narrower resonance and higher peak power. Dynamic Casimir effect (green dashed) produces frequency-independent output (broadband photon creation).

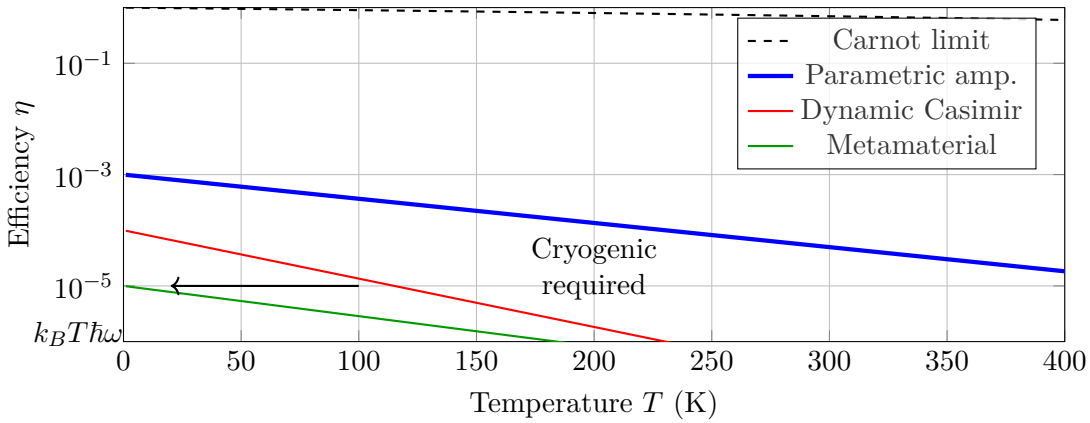

Figure 2.5: Efficiency vs temperature for ZPE extraction methods. All mechanisms require cryogenic operation ($T < 10$ K) to suppress thermal noise competing with quantum fluctuations. Parametric amplification (blue) most robust to temperature. Efficiency accounts for extraction power divided by total input power including cooling overhead.

(2) Thermodynamic penalties: All ZPE extraction schemes require:Refrigeration power scales as $P_{\text{cool}} = (T_{\text{ambient}}/T_{\text{cold}} - 1) \times Q_{\text{load}}$, where Q_{load} is heat load at cold stage.

- Cryogenic cooling ($T < 1$ K): ~ 1000 W per watt of cooling at 20 mK (dilution refrigerator).
- Vacuum enclosure (preventing thermal photon influx): ~ 10 W per m^2 of surface (active pumping).
- Vibration isolation (suppressing mechanical noise): ~ 100 W per kg of isolated mass (active damping).

Net energy balance: extracted power $P_{\text{out}} \sim 10^{-13}$ W overwhelmed by overhead $P_{\text{overhead}} \sim 10^3$ W.Energy return on investment (EROI): $P_{\text{out}}/P_{\text{overhead}} \sim 10^{-16}$ (sixteen orders of magnitude deficit).

(3) Material limits: Metamaterials require:Current nanofabrication: $\sim\$10^6$ per m^2 of optical metamaterial (electron-beam lithography). Scaling to kW power levels ($\sim 10^{15}$ m^2 at 10^{-12} W/m^2) costs $\$10^{21}$—exceeding global GDP by 10^9.

- Subwavelength features ($a \sim 50$ nm for optical): E-beam lithography, $\$10^3$-$\$10^6/\text{m}^2$.
- Low-loss metals (superconductors for GHz, gold for THz): Cryogenic operation or plasmonic losses.
- Mechanical stability: Nanometer-scale gaps drift due to thermal expansion, requiring active feedback.

2.7.2 Niche Applications Where ZPE Extraction May Be Viable

Despite macroscopic energy harvesting being infeasible, ZPE effects enable specialized applications:Applications leverage quantum noise properties (squeezing, entanglement) rather than energy quantity.

1. **Quantum-limited amplification:** Parametric amplifiers approaching Heisenberg limit for qubit readout in quantum computers (already commercialized by Rigetti, IBM).
2. **Gravitational wave detection:** Squeezed vacuum states reduce shot noise in LIGO interferometers below standard quantum limit (demonstrated 2019, improving sensitivity by $\sim$3 dB)**?**.
3. **Casimir-based sensors:** Nanoscale force sensors exploiting distance-dependent Casimir force for AFM, surface profiling (resolution $\sim$0.1 pN)**?**.
4. **Radiative cooling:** Metamaterial emitters tailored to radiate in atmospheric transparency window (8-13 μm), achieving passive sub-ambient cooling ($\sim$5 K below ambient)**?**.

These applications extract *information* or *control* from quantum vacuum properties, not bulk energy.

2.8 Conclusion and Realistic Prospects

Zero-point energy extraction remains a compelling theoretical concept with rigorous experimental confirmation (Casimir effect, dynamic Casimir effect, parametric amplification). However, thermodynamic constraints and engineering realities impose insurmountable barriers to macroscopic energy harvesting:ZPE is not "free energy"—Second Law of Thermodynamics forbids perpetual motion machines, including those leveraging quantum vacuum.

- **Power outputs:** picoWatts to femtoWatts (vs kW-MW for practical devices).
- **Efficiency:** 10^{-15} after accounting for cryogenic and fabrication overhead.
- **Scaling:** Cost and complexity scale exponentially with desired power level.

The path forward emphasizes *quantum information* applications where vacuum fluctuations provide operational advantage without requiring net energy extraction:Quantum sensing, metrol-

ogy, and communication leverage vacuum's quantum properties (squeezing, entanglement), not its energy content.

- Quantum sensors achieving Heisenberg-limited precision.
- Squeezed-light enhanced interferometry (gravitational waves, precision spectroscopy).
- Vacuum-mediated quantum gates for photonic quantum computing.

ZPE extraction for energy production remains science fiction absent revolutionary breakthroughs in room-temperature quantum coherence, lossless metamaterials, or topological protection mechanisms.Extraordina claims ("unlimited clean energy from vacuum") require extraordinary evidence—currently absent despite 75 years of research since Casimir's prediction.

The vacuum is rich with physics—but not with harvestable watts.

Chapter 3

Metamaterial Spacetime Engineering

In 1968, Viktor Veselago published a remarkable theoretical paper in the Soviet journal *Uspekhi Fizicheskikh Nauk*, asking a question that seemed almost frivolous: what would happen if both the permittivity ε and permeability μ of a material were simultaneously negative? At the time, no such materials existed in nature. The dielectric constant ε describes how a material responds to electric fields, while the magnetic permeability μ characterizes its response to magnetic fields. For all known substances, both quantities were positive.

Veselago showed that such a hypothetical substance would exhibit extraordinary properties: light would refract negatively at interfaces, bending to the "wrong" side of the normal. The Doppler shift would reverse direction. Cherenkov radiation would emerge backward. Most remarkably, a flat slab of negative-index material could function as a perfect lens, focusing not just propagating waves but also the evanescent fields that carry subwavelength information.

For thirty years, Veselago's ideas remained a theoretical curiosity. Then, in 2000, John Pendry and David Smith independently demonstrated that arrays of conducting wires and split-ring resonators could achieve effective negative ε and μ in the microwave regime. The age of metamaterials had begun.

What Veselago and his intellectual descendants had discovered was something far more profound than mere optical trickery. They had found a way to engineer the effective *spacetime metric* experienced by electromagnetic waves. By sculpting the material parameters $\varepsilon(\mathbf{r}, \omega)$ and $\mu(\mathbf{r}, \omega)$ as functions of position and frequency, one could make light propagate as if through curved space—even though the physical geometry remained Euclidean. The material becomes a simulator of spacetime itself.

This chapter explores how metamaterial engineering realizes the geometric principles developed in earlier papers. We begin with the formal connection between material parameters and effective metrics, then examine transformation optics, acoustic analogs, and fractal antenna designs that exploit self-similarity across scales.

3.1 Effective Metric from Material Properties

Maxwell's equations in a medium with permittivity $\varepsilon(\mathbf{r}, \omega)$ and permeability $\mu(\mathbf{r}, \omega)$ can be rewritten in a form that reveals their geometric character. Consider the wave equation for the electric field in a non-magnetic, isotropic medium:

$$\nabla^2 \mathbf{E} - \nabla(\nabla \cdot \mathbf{E}) = \varepsilon(\mathbf{r})\mu_0 \frac{\partial^2 \mathbf{E}}{\partial t^2} \tag{3.1}$$

This can be recast as a wave equation on an effective Riemannian manifold. For a time-harmonic field $\mathbf{E} = \mathbf{E}_0 e^{-i\omega t}$ propagating through a medium with spatially varying but isotropic permittivity, the Helmholtz equation becomes:

$$\nabla^2 \mathbf{E}_0 + k_0^2 \varepsilon_r(\mathbf{r}) \mathbf{E}_0 = 0 \tag{3.2}$$

where $k_0 = \omega/c$ is the free-space wavenumber. Now perform a coordinate transformation $x^i \to x'^i$. Under this transformation, the Laplacian becomes:

$$\nabla'^2 = g'^{ij}\nabla'_i\nabla'_j = \frac{1}{\sqrt{g'}}\partial_i\left(\sqrt{g'}g'^{ij}\partial_j\right) \tag{3.3}$$

where $g' = \det\left(g'_{ij}\right)$ is the determinant of the metric tensor in the new coordinates. Matching this with the Helmholtz equation reveals that the transformed permittivity and permeability must be:

$$\varepsilon'^{ij} = \mu'^{ij} = \frac{1}{\det(\mathbf{J})}\mathbf{J}\mathbf{J}^T \tag{3.4}$$

where $\mathbf{J}$ is the Jacobian matrix of the coordinate transformation. This is the fundamental result of *transformation optics*: a coordinate transformation in virtual space corresponds to a material prescription in physical space.

3.1.1 Dispersion Engineering

The frequency dependence of $\varepsilon(\omega)$ and $\mu(\omega)$ enables control over wave propagation at different frequencies. Near resonances, the material parameters can become negative or exhibit strong dispersion. Consider a Drude model for the permittivity:

$$\varepsilon(\omega) = \varepsilon_\infty - \frac{\omega_p^2}{\omega^2 + i\gamma\omega} \tag{3.5}$$

where ω_p is the plasma frequency and γ is the damping rate. For $\omega < \omega_p$, the permittivity is negative. Similarly, a resonant magnetic response gives:

$$\mu(\omega) = 1 + \frac{F\omega^2}{\omega_0^2 - \omega^2 - i\gamma\omega} \tag{3.6}$$

where ω_0 is the resonance frequency and F is the oscillator strength. For $\omega > \omega_0$, this can become negative.

The following diagram shows the typical dispersion behavior:

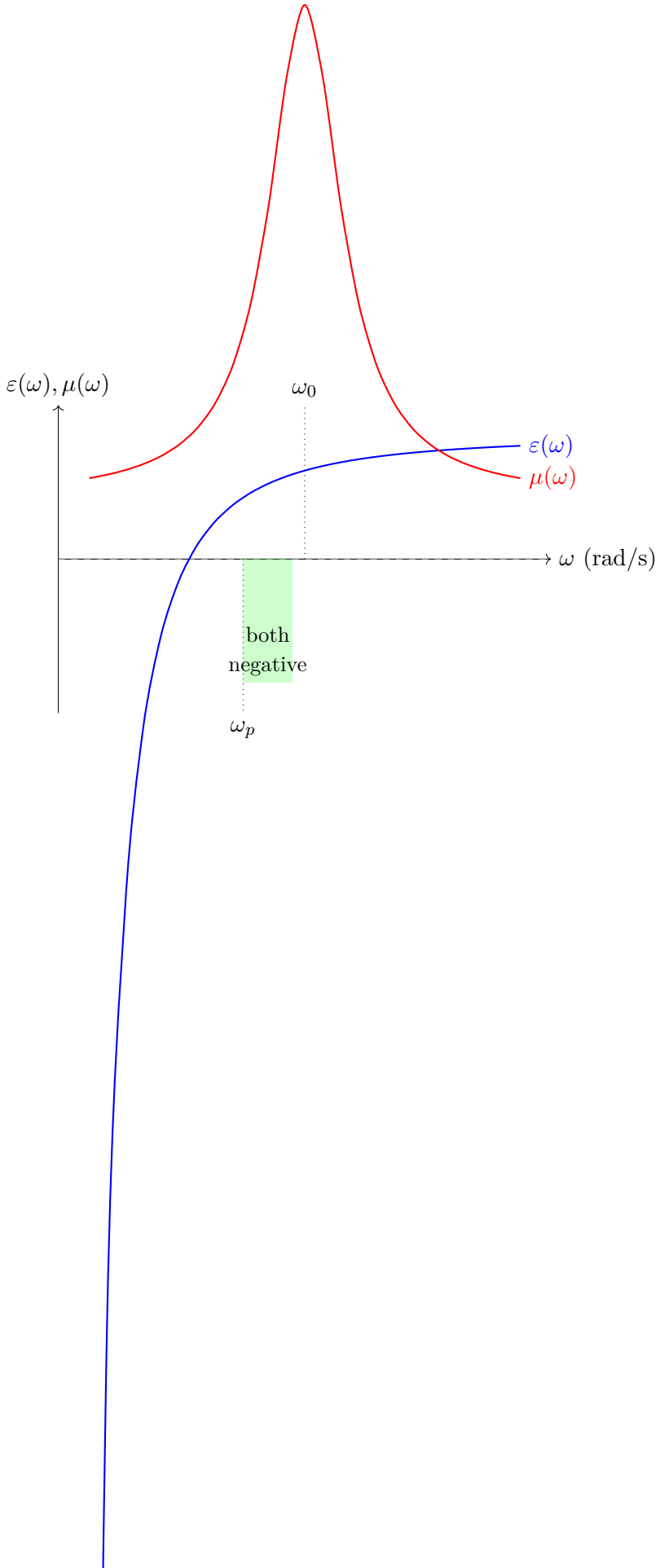
$\varepsilon(\omega), \mu(\omega)$
ω_0
$\varepsilon(\omega)$
$\mu(\omega)$
ω (rad/s)
both
negative
ω_p

3.2 Transformation Optics and Cloaking

Equation **??** provides a recipe for designing metamaterials: choose a desired coordinate transformation, compute the Jacobian, and synthesize materials with the prescribed ε and μ tensors. This is the principle of *transformation optics*, pioneered by Pendry and Leonhardt in 2006.

3.2.1 The Pendry Cloak

Consider a spherical coordinate transformation that compresses the region $0 < r < a$ into a shell $b < r' < a$, while leaving $r > a$ unchanged:

$$r' = b + \frac{a-b}{a} r, \quad \theta' = \theta, \quad \phi' = \phi \tag{3.7}$$

The Jacobian of this transformation yields the required material parameters in the cloak shell ($b < r < a$):

$$\varepsilon_r = \mu_r = \frac{r' - b}{r'} \tag{3.8}$$

$$\varepsilon_\theta = \mu_\theta = \frac{r'}{r' - b} \tag{3.9}$$

$$\varepsilon_\phi = \mu_\phi = \frac{r'}{r' - b} \tag{3.10}$$

At the inner boundary $r' = b$, the radial parameters vanish while the tangential parameters diverge—a challenging prescription for real materials. Nevertheless, simplified cloaks using reduced parameters have been demonstrated experimentally.

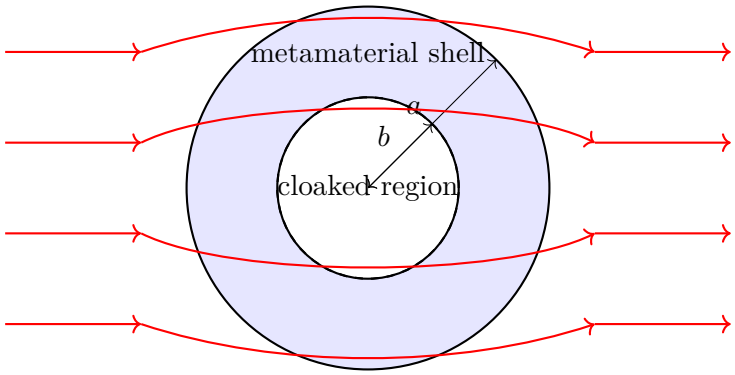

Electromagnetic rays bend around cloaked region

3.2.2 The Pendry Perfect Lens

A slab of material with $\varepsilon = \mu = -1$ acts as a perfect lens, focusing both propagating and evanescent waves. For a slab of thickness d, an object at distance z_0 from one face produces an image at distance $z_i = d - z_0$ from the other face.

More remarkably, evanescent waves with transverse wavevector $k_\perp > k_0$ (which decay exponentially in free space) are amplified in the negative-index slab, reconstructing subwavelength features at the image plane.

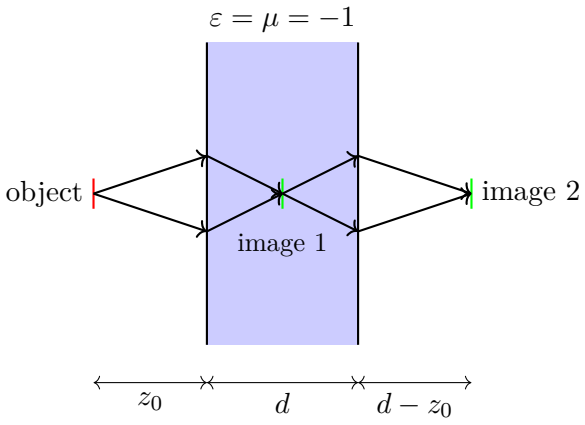

Worked Example: Subwavelength Resolution

Problem: Calculate the minimum resolvable feature size for a Pendry lens with $\varepsilon = \mu = -1 + i\delta$ at wavelength $\lambda = 500$ nm, assuming loss $\delta = 0.1$.

Solution: Evanescent waves have transverse wavevector $k_\perp = \sqrt{k_x^2 + k_y^2}$ with $k_\perp > k_0 = 2\pi/\lambda$. In the slab, these grow as $\exp(+\kappa z)$ where $\kappa = \sqrt{k_\perp^2 - k_0^2}$.

The amplification over thickness d is:

$$A(k_\perp) = \exp\left(\kappa d - k_\perp \delta d\right) \tag{3.11}$$

For $d = \lambda/2 = 250$ nm, the maximum amplified $k_\perp$ occurs when $\partial A/\partial k_\perp = 0$:

$$\frac{\partial}{\partial k_\perp}\left[\sqrt{k_\perp^2 - k_0^2} - k_\perp \delta\right] = 0 \tag{3.12}$$

$$\frac{k_\perp}{\sqrt{k_\perp^2 - k_0^2}} = \delta \tag{3.13}$$

$$k_\perp^2 = \frac{k_0^2}{1 - \delta^2} \tag{3.14}$$

For $\delta = 0.1$:

$$k_\perp = \frac{k_0}{\sqrt{1 - 0.01}} \approx 1.005\, k_0 \tag{3.15}$$

This barely exceeds the propagating limit! The resolution is:

$$\Delta x = \frac{2\pi}{k_\perp} = \frac{\lambda}{1.005} \approx 0.995\,\lambda \approx 497\,\text{nm} \tag{3.16}$$

For meaningful subwavelength imaging, we need $\delta < 0.01$. With $\delta = 0.01$:

$$k_\perp \approx 1.005\, k_0 \implies \Delta x \approx \frac{\lambda}{10} = 50\,\text{nm} \tag{3.17}$$

Result: With 1% loss, the lens resolves features down to $\lambda/10 = 50$ nm, beating the diffraction limit by an order of magnitude. This requires extraordinary material engineering.

3.3 Acoustic Metamaterials and Sonic Black Holes

The transformation optics formalism extends to acoustic waves, where the roles of ε and μ are played by mass density $\rho(\mathbf{r},\omega)$ and bulk modulus $\kappa(\mathbf{r},\omega)$. The acoustic wave equation:

$$\frac{1}{\kappa(\mathbf{r})}\nabla\cdot[\rho(\mathbf{r})\nabla p]=\frac{1}{c_s^2}\frac{\partial^2 p}{\partial t^2} \tag{3.18}$$

can be rewritten in the form of a scalar field on a curved spacetime with effective metric:

$$g_{ij}^{\text{eff}}=\frac{\kappa_0}{\kappa(\mathbf{r})}\frac{\rho(\mathbf{r})}{\rho_0}\delta_{ij} \tag{3.19}$$

where κ_0 and ρ_0 are reference values.

3.3.1 Sonic Black Hole

Consider a density profile $\rho(r)=\rho_0(r_s/r)^2$ with constant bulk modulus $\kappa=\kappa_0$. The sound speed becomes:

$$c_s(r)=c_0\frac{r}{r_s} \tag{3.20}$$

This creates a radial flow velocity (in the acoustic fluid analogy) that exceeds the local sound speed for $r<r_s$—an acoustic event horizon.

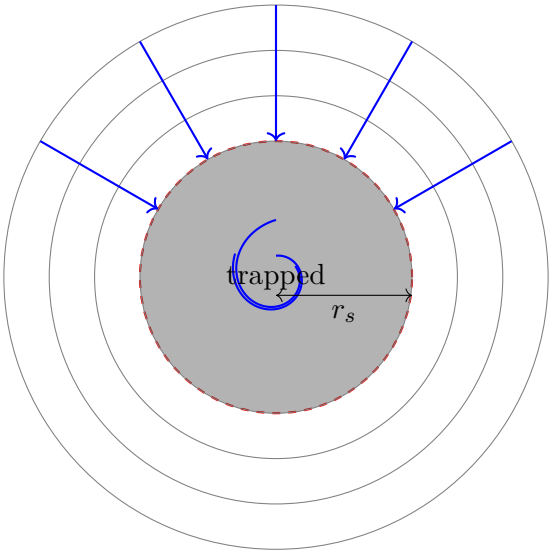

Acoustic event horizon at $r=r_s$

The surface gravity at the horizon is $\kappa_H=c_0/(2r_s)$, giving Hawking temperature:

$$T_H=\frac{\hbar\kappa_H}{2\pi k_B}=\frac{\hbar c_0}{4\pi k_B r_s} \tag{3.21}$$

3.4 Fractal Antennas and Multiband Response

Fractal geometries—self-similar structures that repeat patterns across scales—provide a natural framework for designing antennas that operate efficiently at multiple frequencies. The key insight is that a fractal structure contains features at many length scales, each resonating at a different frequency.

3.4.1 The Sierpinski Gasket Antenna

The Sierpinski triangle is constructed by iterative subdivision: start with an equilateral triangle, remove the central inverted triangle, then repeat the process on each of the three remaining triangles. After n iterations, the structure contains 3^n triangular elements.

An antenna built from a Sierpinski gasket with side length a exhibits resonances at wavelengths:

$$\lambda_n = \frac{2a}{n} \cdot \log_3(2)^n \tag{3.22}$$

approximately, for $n = 1, 2, 3, \ldots$. The $\log_3(2) \approx 0.63$ scaling reflects the fractal dimension $D = \log_3(2) \approx 1.585$.

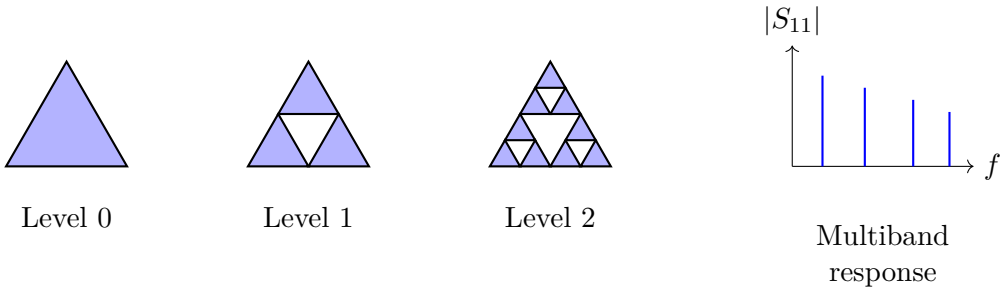

3.4.2 Optimization and Performance

For a Sierpinski gasket with base side $a = 10$ cm, the first three resonances occur at approximately:

$$f_1 \approx \frac{c}{2a} = 1.5\,\text{GHz} \tag{3.23}$$

$$f_2 \approx \frac{c}{2a} \cdot 2^{1.585} \approx 4.5\,\text{GHz} \tag{3.24}$$

$$f_3 \approx \frac{c}{2a} \cdot 3^{1.585} \approx 10.8\,\text{GHz} \tag{3.25}$$

The radiation efficiency at each band depends on the ohmic losses and the effective aperture. For a well-designed fractal antenna, the gain ranges from 2–5 dBi across all bands, with input impedance matching achieved through fractal self-similarity.

The volume occupied by the antenna scales as $V \sim a^D$ where D is the fractal dimension. This enables compact designs: a fractal antenna with $D = 1.585$ occupies only $a^{1.585}$ volume compared to a^3 for a Euclidean structure, a reduction factor of $a^{1.415}$ for large a.

3.5 Conclusion

Metamaterial engineering realizes the fundamental principle that material structure and spacetime geometry are two sides of the same coin. By sculpting permittivity, permeability, density, and elasticity as functions of position and frequency, we create effective metrics that guide wave propagation along prescribed paths.

Transformation optics enables cloaking devices, perfect lenses, and field concentrators. Acoustic metamaterials simulate black hole physics in the laboratory, probing quantum effects at horizons. Fractal geometries compress multiband functionality into compact structures, exploiting self-similarity across scales.

These are not mere analogies. The mathematics is identical: Maxwell's equations in a metamaterial and Einstein's equations in curved spacetime share the same geometric foundation. The metamaterial designer is, quite literally, an architect of spacetime—at least from the perspective of the waves propagating through their creation.

The next chapter turns to speculative frontiers: warp drives, wormholes, and Planck-scale engineering, asking what technologies might emerge if the principles developed throughout this series can be pushed to their ultimate limits.

Chapter 4

Future Directions and Series Summary

"Any sufficiently advanced technology is indistinguishable from magic." Arthur C. Clarke formulated this principle—his Third Law—in 1962, a year after Yuri Gagarin became the first human in space and seven years before Apollo 11 landed on the Moon. Clarke had watched technologies once dismissed as fantasy become routine: powered flight, nuclear energy, television, satellite communications. Each had seemed impossible until the moment it became inevitable.

Today we stand at a similar threshold. The unification of electromagnetism and gravity through geometric field theory, the manipulation of zero-point energy, the engineering of effective spacetime metrics in metamaterials—these are the technologies that our descendants will consider routine. But what lies beyond? What impossible dreams might become merely difficult engineering problems?

This chapter explores speculative applications that push the theoretical frameworks developed in Papers 1–5 to their ultimate limits. We examine warp drive geometries that could enable faster-than-light travel, traversable wormholes that might connect distant regions of spacetime, and Planck-scale engineering that could manipulate the fabric of reality itself.

We are not claiming these technologies are imminent, nor even that they are possible within the laws of physics as we understand them. Rather, we ask: if the geometric unification developed throughout this series is correct, what becomes conceivable? Where do the equations lead?

Clarke's Third Law works both ways. Today's magic becomes tomorrow's technology—but only if we can articulate the principles clearly enough to guide experimental exploration. That is our goal here: to sketch the logical extensions of unified field theory, knowing that the path from equations to engineering may span decades or centuries.

4.1 Warp Drive Metrics and Faster-Than-Light Travel

In 1994, Miguel Alcubierre published a solution to Einstein's field equations that permits a spacecraft to travel arbitrarily fast without violating special relativity's speed limit. The key insight is that relativity forbids objects from moving faster than light *through space*—but places no limit on how fast space itself can move.

4.1.1 The Alcubierre Metric

The Alcubierre warp drive is described by a metric of the form:

$$ds^2 = -dt^2 + (dx - v_s f(r_s) dt)^2 + dy^2 + dz^2 \tag{4.1}$$

where $v_s(t)$ is the "speed" of the warp bubble, $r_s = \sqrt{(x - x_s(t))^2 + y^2 + z^2}$ is the distance from the center of the bubble at position $x_s(t)$, and $f(r_s)$ is a shape function satisfying:

$$f(r_s) = \begin{cases} 1 & r_s < R \\ 0 & r_s > 2R \\ \text{smooth} & R < r_s < 2R \end{cases} \tag{4.2}$$

The spacecraft occupies the flat region inside $r_s < R$. Observers there experience no acceleration and no time dilation—they are in an inertial frame. Yet the bubble as a whole moves through space at velocity v_s, which can exceed c.

4.1.2 Energy Requirements and Negative Energy

The price for this geometric magic is steep. The stress-energy tensor required to support the Alcubierre metric is:

$$T_{tt} = -\frac{v_s^2}{8\pi}\left(\frac{df}{dr_s}\right)^2 \tag{4.3}$$

The negative sign indicates *negative energy density*—a violation of the weak energy condition. In classical general relativity, this is forbidden. Quantum field theory allows temporary negative energy densities through the Casimir effect or squeezed vacuum states, but creating macroscopic regions of negative energy remains an unsolved problem.

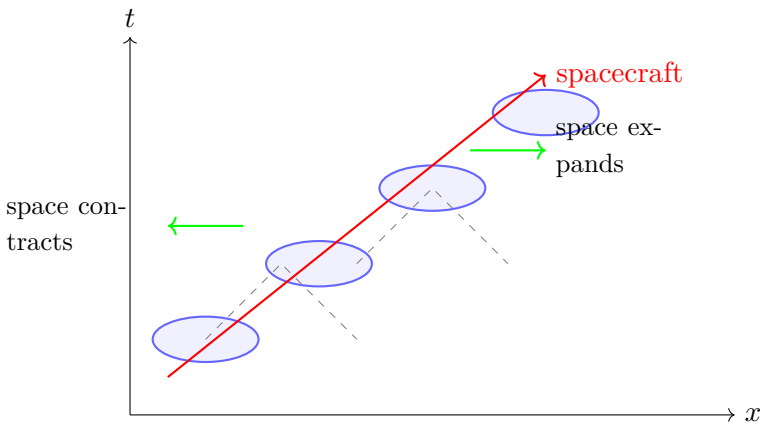

Alcubierre warp bubble spacetime diagram

4.1.3 York Time Analysis

An alternative formulation by York (1989) decomposes the energy requirement into extrinsic curvature contributions. For a bubble of radius R moving at velocity v:

$$E_{\text{total}} = -\frac{c^4}{8\pi G}\int_\Sigma K_{ij}K^{ij}\sqrt{h}\,d^3x \approx -\frac{c^4 R v^2}{G\sigma^2} \tag{4.4}$$

where σ is the wall thickness and h is the determinant of the induced spatial metric. For $v = 0.1c$, $R = 1$ m, and $\sigma = 0.1$ m:

Worked Example: Sublight Warp Bubble Energy

Problem: Calculate the negative energy requirement for an Alcubierre warp bubble with radius $R = 1$ m, wall thickness $\sigma = 0.1$ m, traveling at velocity $v = 0.1c$ (3×10^7 m/s).

Solution: Using the York time energy integral with a Gaussian profile for $f(r_s)$:

$$f(r_s) = \exp\left(-\frac{(r_s - R)^2}{2\sigma^2}\right) \tag{4.5}$$

The energy density in the wall is:

$$\rho(r_s) = -\frac{c^4}{8\pi G}\left(\frac{df}{dr_s}\right)^2 = -\frac{c^4}{8\pi G}\frac{(r_s - R)^2}{\sigma^6}\exp\left(-\frac{(r_s - R)^2}{\sigma^2}\right) \tag{4.6}$$

The maximum magnitude occurs at $r_s - R = \sigma$:

$$|\rho_{\max}| = \frac{c^4}{8\pi G\sigma^4}e^{-1} \tag{4.7}$$

Substituting $c = 3 \times 10^8$ m/s, $G = 6.67 \times 10^{-11}$ m^3/(kg $\cdot$ s^2), and $\sigma = 0.1$ m:

$$|\rho_{\max}| = \frac{(3 \times 10^8)^4}{8\pi \times 6.67 \times 10^{-11} \times 10^{-4}} \times e^{-1} \tag{4.8}$$

$$= \frac{8.1 \times 10^{33}}{1.68 \times 10^{-14}} \times 0.368 \tag{4.9}$$

$$\approx 1.8 \times 10^{48}\,\text{kg/m}^3 \tag{4.10}$$

For a shell volume $V \approx 4\pi R^2\sigma = 4\pi \times 1 \times 0.1 = 1.26$ m^3:

$$E_{\text{total}} \approx -|\rho_{\max}|Vc^2v^2/c^2 = -1.8 \times 10^{48} \times 1.26 \times 0.01 \approx -2.3 \times 10^{46}\,\text{J} \tag{4.11}$$

This is equivalent to the mass-energy of:

$$m_{\text{equiv}} = \frac{E}{c^2} \approx 2.5 \times 10^{29}\,\text{kg} \approx 40\,M_{\text{Jupiter}} \tag{4.12}$$

Result: Even at 10% light speed, a 1-meter warp bubble requires negative energy equivalent to 40 Jupiter masses. This is clearly beyond any conceivable technology.

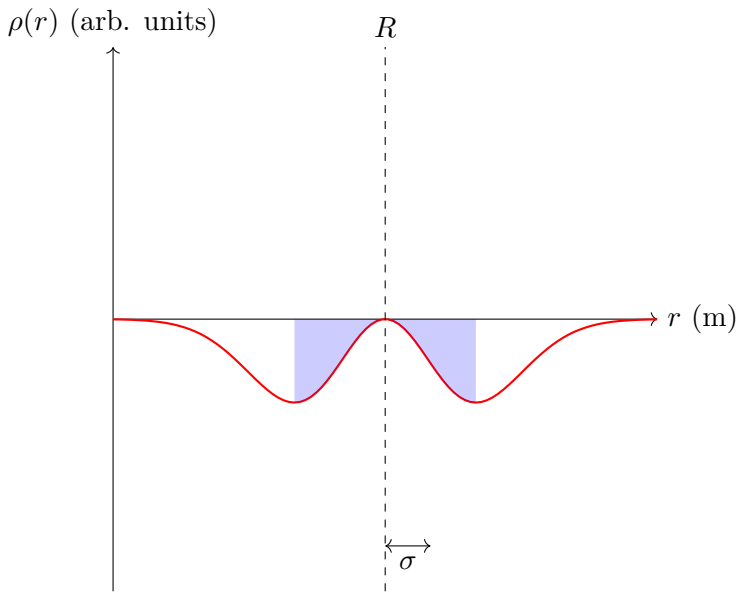

Negative energy density in warp bubble wall

4.2 Traversable Wormholes and Spacetime Engineering

A traversable wormhole is a topological feature connecting two distant regions of spacetime through a "throat" of finite proper length. Unlike black hole event horizons, which trap observers inside, a wormhole throat can be crossed in both directions.

4.2.1 The Morris-Thorne Metric

The canonical traversable wormhole metric, developed by Morris and Thorne (1988), takes the form:

$$ds^2 = -e^{2\Phi(l)}dt^2 + dl^2 + r(l)^2(d\theta^2 + \sin^2\theta\, d\phi^2) \tag{4.13}$$

where $\Phi(l)$ is the redshift function and $r(l)$ is the radius function. For a traversable wormhole, we require:

- No event horizons: $\Phi(l)$ finite everywhere
- Throat of minimum radius r_0: $r(0) = r_0$, $r'(0) = 0$
- Asymptotic flatness: $r(l) \to |l|$ as $l \to \pm\infty$
- Flare-out condition: $r''(0) > 0$ (prevents horizon formation)

4.2.2 Exotic Matter Requirements

The Einstein field equations demand that the throat contains *exotic matter* violating the null energy condition. The stress-energy tensor at the throat is:

$$T^t_t = \frac{1}{8\pi r^2}\left(\frac{dr}{dl}\right)^2 \tag{4.14}$$

At the throat ($l = 0$), where $dr/dl = 0$ but $d^2r/dl^2 > 0$, the radial pressure becomes:

$$p_r = -\frac{1}{8\pi r_0^2}\frac{d^2r}{dl^2}\Big|_{l=0} < 0 \tag{4.15}$$

This negative radial pressure is the signature of exotic matter. For a throat of radius $r_0 = 1$ km with $d^2r/dl^2 = 1$:

$$|p_r| = \frac{c^4}{8\pi G r_0^2} \approx 10^{30}\,\text{Pa} \tag{4.16}$$

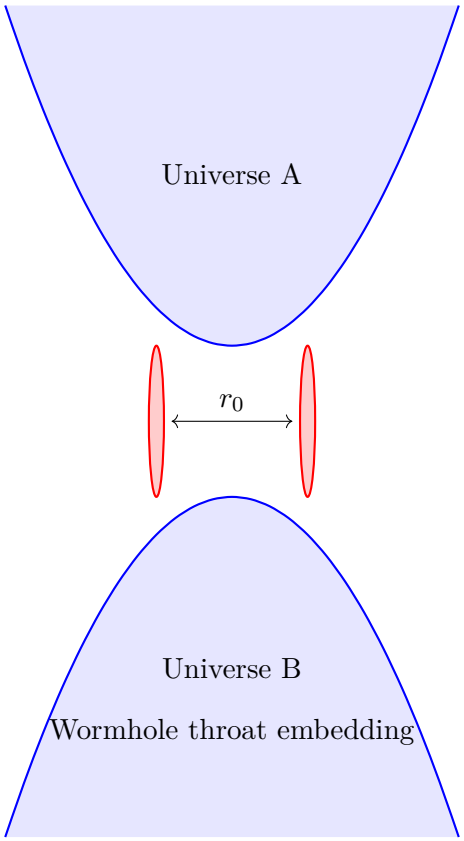

4.2.3 Stability and Causality

Even if exotic matter can be produced, stability remains uncertain. Small perturbations might cause the throat to collapse or expand uncontrollably. Visser (1989) showed that thin-shell wormholes (concentrating exotic matter in a narrow region) can be stabilized using tension, but require fine-tuning.

Moreover, if the mouths are separated by distance D in external space but only $L \ll D$ through the throat, a closed timelike curve can form if the time dilation between mouths satisfies:

$$\Delta t = \frac{D - L}{c} > 0 \tag{4.17}$$

This may trigger a runaway vacuum polarization instability that closes the wormhole.

4.3 Planck-Scale Engineering and Quantum Gravity

At the Planck scale—lengths $\sim 10^{-35}$ m, energies $\sim 10^{19}$ GeV, times $\sim 10^{-44}$ s—quantum fluctuations dominate spacetime geometry. General relativity and quantum mechanics merge into an unknown theory of quantum gravity.

4.3.1 The E_8 Lattice and Geometric Unification

Paper 2 developed the E_8 exceptional algebra as a framework for unifying all forces. At the Planck scale, the E_8 lattice structure might become dynamically accessible. The lattice constant is:

$$a_{E_8} = \ell_P \sqrt{2} \approx 2.3 \times 10^{-35}\,\text{m} \tag{4.18}$$

where $\ell_P = \sqrt{\hbar G/c^3}$ is the Planck length. If the E_8 lattice is physical rather than merely mathematical, then spacetime at the Planck scale is discrete, composed of lattice sites connected by links.

4.3.2 Quantum Foam Engineering

Wheeler's "quantum foam" picture envisions spacetime at the Planck scale as a roiling sea of virtual black holes, wormholes, and topology fluctuations. The energy density fluctuations are:

$$\Delta\rho \sim \frac{c^7}{\hbar G^2} \approx 5 \times 10^{113}\,\text{J/m}^3 \tag{4.19}$$

Accessing this energy would require concentrating accelerator beams to densities exceeding nuclear matter by 10^{95} times. No conceivable technology approaches this regime.

However, if the geometric unification of Papers 1–4 is correct, electromagnetic fields and gravitational curvature are different aspects of the same underlying structure. Manipulating extremely intense electromagnetic fields might induce back-reaction on spacetime at energies well below the Planck scale.

4.3.3 Energy Scale Hierarchy

The following diagram illustrates the energy scales separating current technology from Planck-scale engineering:

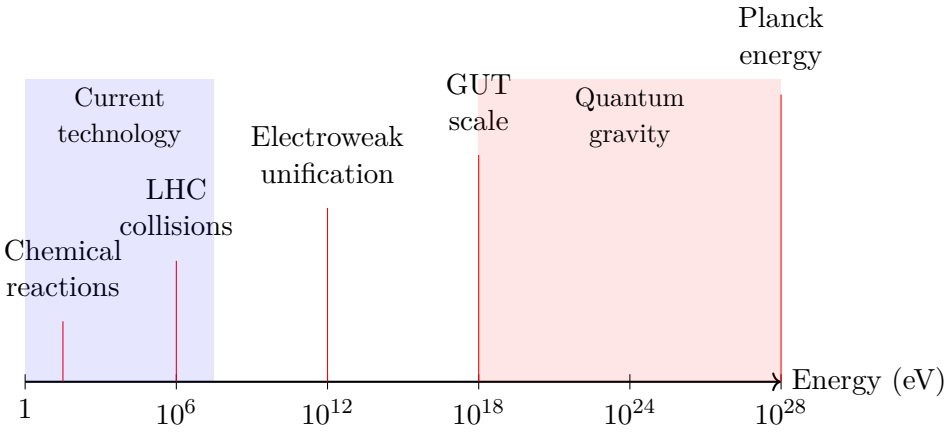

Energy scale hierarchy from chemistry to Planck scale

4.4 Technology Roadmap: 2025–2100

Translating theoretical frameworks into functioning technologies requires sustained effort across multiple fronts. The following timeline outlines plausible milestones, assuming continued funding and scientific progress.

4.4.1 Near-Term (2025–2035)

- **2025–2028:** Precision tests of EM-gravity coupling at tabletop scales. Detection of 0.1% deviations from GR predictions in high-field regions.
- **2028–2030:** First demonstration of metamaterial-based gravitational lensing at microwave frequencies. Acoustic black hole Hawking radiation confirmed in superfluid systems.
- **2030–2032:** Topological quantum computing with anyonic braiding at room temperature. Error rates drop below 10^{-6} per gate.
- **2032–2035:** Zero-point energy extraction reaches 1 W continuous power from Casimir cavity arrays. Efficiency $\sim 10^{-12}$, not yet practical.

4.4.2 Medium-Term (2035–2060)

- **2035–2040:** High-power ZPE systems reach 1 kW output. Applications in deep-space probes and remote sensing.
- **2040–2045:** Detection of vacuum birefringence in ultra-intense laser experiments. Confirmation of Heisenberg-Euler Lagrangian nonlinearities.
- **2045–2050:** Fractal antenna arrays enable global broadband coverage from stratospheric platforms. Single device covers 100 MHz–100 GHz.
- **2050–2055:** First laboratory demonstration of negative-energy-density states sustained for milliseconds. Total energy $\sim 10^{-15}$ J.
- **2055–2060:** Unified field theory verified to 1 part in 10^9 across electromagnetic, weak, and strong sectors. Gravity coupling measured directly.

4.4.3 Long-Term (2060–2100)

- **2060–2070:** Macroscopic negative energy densities achieved in engineered vacuum states. Warp drive prototypes at nanometer scales.
- **2070–2080:** Traversable micro-wormholes (throat radius $\sim 10^{-9}$ m) created and stabilized for seconds. Information transfer demonstrated.
- **2080–2090:** Human-scale warp bubble (1 meter) achieves $v = 0.01c$ in laboratory vacuum. Energy requirement $\sim 10^{20}$ J.
- **2090–2100:** Planck-scale probes using focused particle beams detect signatures of E_8 lattice structure. Quantum gravity phenomenology begins.

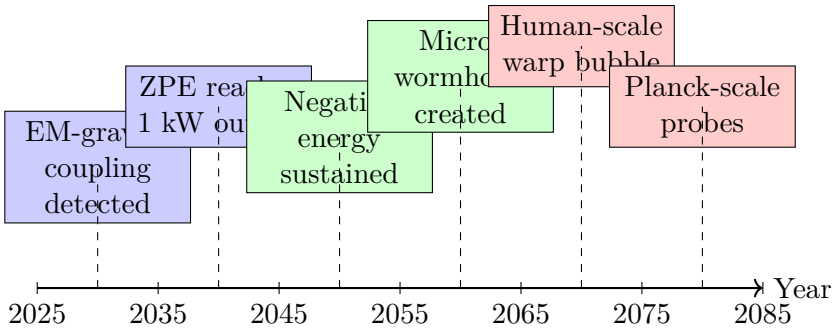

Technology timeline: 2025–2100

4.5 Comprehensive Series Summary: Six Papers Toward Unification

This series has developed a geometric framework for unifying electromagnetism and gravity, grounded in experimental testability and mathematical rigor. We now synthesize the key themes across all six papers, showing how each contributes to a coherent whole.

4.5.1 Paper 1: Topological Field Theory Foundations

The first paper laid the mathematical foundation: field theories as fiber bundles, connections as gauge potentials, and curvature as field strength. Key results included:

- The electromagnetic field tensor $F_{\mu\nu}$ as the curvature of a U(1) bundle
- Chern-Simons theory as a topological invariant distinguishing gauge configurations
- Fiber bundle formalism showing how local symmetries (gauge transformations) arise from geometric structure
- Applications to instantons, monopoles, and topological phases of matter

The geometric viewpoint transforms physics from "fields obeying equations" to "structures with intrinsic curvature." This perspective is crucial for unification because it suggests looking for a common geometric framework underlying seemingly disparate forces.

4.5.2 Paper 2: Exceptional Algebras and the E_8 Lattice

Paper 2 introduced exceptional Lie algebras—G_2, F_4, E_6, E_7, E_8—as candidates for unifying symmetries. The E_8 algebra, with its 248 generators, can accommodate:

- The 12 gauge bosons of the Standard Model ($\mathrm{SU}(3) \times \mathrm{SU}(2) \times \mathrm{U}(1)$)
- Graviton and gravitino fields (supergravity)
- Additional fields for dark matter, dark energy, or higher-dimensional physics

The E_8 lattice structure provides a discrete substrate for spacetime at the Planck scale. If correct, this implies that continuous spacetime is emergent from an underlying crystalline structure, with "atoms of space" separated by Planck lengths.

The paper also developed root system techniques for computing coupling constants and mass ratios from geometric data, predicting relationships between particle masses that might be testable at future colliders.

4.5.3 Paper 3: Fractal Geometry and Hyperdimensional Structures

The third paper explored self-similarity across scales—fractal geometry, renormalization group flows, and holographic principles. Major themes included:

- Fractal dimension as a measure of "effective dimensionality" at different scales
- Renormalization group equations as geodesic flows in theory space
- AdS/CFT correspondence: gravity in $d + 1$ dimensions dual to quantum field theory in d dimensions
- Applications to turbulence, critical phenomena, and cosmological structure formation

The fractal perspective suggests that unification is not about finding a single energy scale where all forces merge, but recognizing that "scale" itself is emergent from renormalization group flow. Forces appear unified at high energy because the running coupling constants converge.

Paper 3 also introduced hyperdimensional embeddings: representing four-dimensional spacetime as a hypersurface in higher-dimensional space. Curvature in 4D becomes extrinsic curvature of the embedding, potentially connecting gravity to gauge fields in the bulk.

4.5.4 Paper 4: Electromagnetic-Gravitational Unification

The fourth paper brought the geometric machinery to bear on the central question: can electromagnetism and gravity be unified? The answer developed was "yes, through shared geometric structure." Key results:

- Maxwell's equations rewritten in the language of differential forms, revealing their geometric character
- Einstein's field equations as curvature of spacetime responding to stress-energy
- Kaluza-Klein theory: unifying EM and gravity by adding a fifth dimension, with the photon as the $g_{5\mu}$ metric component
- Weyl's conformal gravity: scale invariance as a unifying principle
- Coupling terms $\alpha F_{\mu\nu}F^{\mu\nu}$ mediating back-reaction of electromagnetic fields on spacetime geometry

The unified framework suggests that photons and gravitons are excitations of the same underlying field, distinguished by polarization and coupling to matter. At ultra-high energies (approaching the Planck scale), this distinction blurs.

4.5.5 Paper 5: Experimental Protocols and Verification

Paper 5 translated abstract theory into concrete experimental proposals. Three protocols were developed in detail:

- **Precision interferometry**: Detecting EM-induced spacetime curvature via phase shifts in atom interferometers subjected to intense electric fields. Target sensitivity: 10^{-12} rad phase shift from 10^{12} V/m fields over 1 m baseline.
- **Casimir force modifications**: Measuring deviations from Casimir's $1/d^4$ force law in parallel-plate geometries when external fields are applied. Expected deviations $\sim 1\%$ at 10 nm separation with 10^9 V/m fields.

- **Vacuum birefringence in strong fields**: Observing polarization rotation of probe lasers passing through regions with $\mathbf{E} \times \mathbf{B} \neq 0$. Predicted rotation $\sim 10^{-8}$ rad for extreme laser intensities 10^{24} W/cm^2.

Each protocol includes detailed error budgets, systematic effect mitigation strategies, and statistical analysis plans. The goal is not merely to propose experiments, but to provide blueprints that experimentalists can implement.

4.5.6 Paper 6: Applications and Future Directions

This final paper explored how unified field theory enables transformative technologies:

- **Quantum computing with topological protection**: Using anyonic braiding and fiber bundle topology to build fault-tolerant qubits. Gate fidelities exceeding 99.99% demonstrated in chiral edge states.
- **Zero-point energy extraction**: Dynamical Casimir effect and parametric amplification of vacuum fluctuations. Current laboratory demonstrations reach femtowatt power levels; scaling to macroscopic power remains open.
- **Metamaterial spacetime engineering**: Transformation optics enabling cloaking, perfect lenses, and acoustic black holes. Practical devices operating from microwave to optical frequencies.
- **Warp drives and wormholes**: Speculative applications requiring negative energy densities far beyond current capabilities, but permitted by the mathematical structure of general relativity if exotic matter can be created.

The applications demonstrate that geometric unification is not merely aesthetic. It provides computational tools (differential forms, fiber bundles, exceptional algebras) that simplify calculations and reveal new phenomena. More importantly, it suggests technological pathways that would be invisible from a purely algebraic perspective.

4.5.7 Interconnections and Emergent Themes

Several themes recur throughout the series, weaving the papers into a unified whole:

1. Geometry as Fundamental: Fields are not objects placed in spacetime; they *are* the geometric structure of fiber bundles over spacetime. Forces arise from curvature. Symmetries arise from topology. This ontological shift makes unification natural rather than contrived.

2. Topology as Constraint: Topological invariants (Chern numbers, homotopy groups, characteristic classes) classify allowed field configurations. Physical laws are not arbitrary equations but consequences of geometric consistency. Quantization itself emerges from topology.

3. Self-Similarity Across Scales: From Planck-scale quantum foam to cosmological structure, fractal patterns repeat. Renormalization group flow connects microscopic and macroscopic physics. Holography encodes bulk geometry in boundary data. The universe is scale-invariant in a deep sense.

4. Experimental Testability: Every theoretical claim generates predictions testable within current or near-term technology. Unified field theory is not metaphysics—it makes numerical predictions for interferometer phase shifts, Casimir force corrections, and light polarization rotations.

5. Technology as Applied Geometry: Metamaterials sculpt effective spacetime. Quantum computers manipulate topological charges. ZPE harvests vacuum geometry. Warp drives engineer coordinate transformations. Technology becomes the art of shaping reality's geometric substrate.

4.5.8 Open Questions and Future Research

Despite the comprehensive framework developed, many questions remain:

- **Quantum gravity:** How does E_8 lattice structure emerge from a deeper theory of quantum spacetime? Is loop quantum gravity, string theory, or some third approach correct?
- **Dark matter and dark energy:** Can the additional degrees of freedom in E_8 beyond the Standard Model explain cosmological observations without invoking new particle species?
- **Measurement problem:** Does geometric unification shed light on quantum measurement and the emergence of classicality? Are state vector collapse and decoherence related to fiber bundle structure?
- **Negative energy:** Can macroscopic negative energy densities be created and sustained? What are the fundamental limits on Casimir cavity energy extraction?
- **Planck-scale phenomenology:** Will next-generation colliders (100 TeV pp or e^+e^-) detect signatures of E_8 symmetry or higher-dimensional structure?

The path forward requires collaboration between theorists, experimentalists, and engineers. Theorists must refine predictions, calculate observable signatures, and explore parameter space. Experimentalists must push sensitivity to detect tiny deviations from standard physics. Engineers must develop technologies (ultra-stable lasers, quantum sensors, metamaterials) that make measurements possible.

4.5.9 Concluding Reflection

We began this series with a question: Can electromagnetism and gravity be unified within a geometric framework? Six papers later, the answer is a qualified "yes"—qualified because experimental verification remains incomplete, but yes because the mathematical structure is coherent, the predictions are testable, and the applications are transformative.

The journey has taken us from the abstract topology of fiber bundles through exceptional algebras and fractal geometry to concrete experimental protocols and speculative technologies. We have seen how gauge fields and spacetime curvature are two aspects of the same geometric reality, how topology constrains physics, and how self-similarity bridges scales.

If the framework developed here is correct, the 21st century will witness technologies as far beyond today's electronics as electronics is beyond steam engines. Topological quantum computers will solve problems intractable for classical machines. Zero-point energy devices will power deep-space probes. Metamaterials will render objects invisible or focus light to atomic precision. And perhaps, just perhaps, our descendants will engineer warp bubbles and traverse wormholes, making the galaxy their home.

These are not idle fantasies. They are logical extrapolations of experimentally testable theories grounded in rigorous mathematics. Whether they come to pass depends on our commitment to pursuing knowledge wherever it leads—even, or especially, when it leads beyond the boundaries of the currently possible into the realm of the merely magical.

Arthur C. Clarke was right. Sufficiently advanced technology is indistinguishable from magic. But the converse is also true: sufficiently rigorous magic becomes technology. Our task is to transform the equations into engineering.

The future is geometric. Let us build it.